



















The Star Formation History and Evolution of the Ultra-Diffuse M81 Satellite, F8D1

ADAM SMERCINA ^{1,*} ERIC F. BELL ² BENJAMIN F. WILLIAMS ³ BENJAMIN N. VELGUTH ^{4,5} SARAH PEARSON ⁶
JEREMY BAILIN ⁷ TSANG KEUNG CHAN ⁸ JULIANNE J. DALCANTON ^{9,3} ROELOF S. DE JONG ¹⁰
RICHARD D'SOUZA ¹¹ ANDREW DOLPHIN ^{12,13} PURAGRA GUHATHAKURTA ¹⁴ KRISTEN B.W. MCQUINN ^{1,15}
ANTONELA MONACHESI ¹⁶ COLIN T. SLATER ³ ELISA TOLOBA ¹⁷ DANIEL R. WEISZ ¹⁸ AND ANDREW WETZEL ¹⁹

¹Space Telescope Science Institute, 3700 San Martin Dr., Baltimore, MD 21218, USA

²Department of Astronomy, University of Michigan, 323 West Hall, 1085 S. University Ave., Ann Arbor, MI, 48105-1107, USA

³Department of Astronomy, University of Washington, Box 351580, Seattle, WA 98195-1580, USA

⁴Department of Astronomy, University of Massachusetts Amherst, 710 North Pleasant Street, Amherst, MA, 01003, USA

⁵Department of Physics and Astronomy, Dartmouth College, Hanover, NH 03755, USA

⁶DARK, Niels Bohr Institute, University of Copenhagen, Jagtvej 155A, 2200 Copenhagen, Denmark

⁷Department of Physics and Astronomy, University of Alabama, Box 870324, Tuscaloosa, AL 35487-0324, USA

⁸Department of Physics, The Chinese University of Hong Kong, Shatin, Hong Kong, China

⁹Center for Computational Astrophysics, Flatiron Institute, 162 Fifth Ave, New York, NY 10010, USA

¹⁰Leibniz-Institut für Astrophysik Potsdam (AIP), An der Sternwarte 16, D-14482 Potsdam, Germany

¹¹Department of Astronomy, University of Michigan, 1085 S. University Ave, Ann Arbor, MI 48109-1107, USA

¹²Raytheon Technologies, 1151 E. Hermans Road, Tucson, AZ 85756, USA

¹³Steward Observatory, University of Arizona, Tucson, AZ 85726, USA

¹⁴UCO/Lick Observatory, Department of Astronomy & Astrophysics, University of California Santa Cruz, 1156 High Street, Santa Cruz, California 95064, USA

¹⁵Department of Physics and Astronomy, Rutgers, The State University of New Jersey, 136 Frelinghuysen Rd, Piscataway, NJ 08854, USA

¹⁶Departamento de Astronomía, Universidad de La Serena, Av. Juan Cisternas 1200 N, La Serena, Chile

¹⁷Department of Physics, University of the Pacific, 3601 Pacific Avenue, Stockton, CA 95211, USA

¹⁸Department of Astronomy, University of California, Berkeley, CA 94720, USA

¹⁹Department of Physics & Astronomy, University of California, Davis, Davis, CA 95616, USA

ABSTRACT

We present deep HST imaging of one of the nearest ultra-diffuse galaxies (UDGs) outside of the Local Group: F8D1, a satellite of M81 known to be tidally disrupting. UDGs are an enigmatic and diverse population, with evolutionary pathways ranging from tidal processing to bursty feedback and high initial angular momentum. To determine F8D1's evolutionary drivers, we resolve stars in F8D1's central ~ 1 kpc and in a parallel field ~ 6 kpc along its major axis to deep photometric limits, reaching below the Red Clump. We also image eight shallower fields along F8D1's major and minor axes. We calculate the star formation history (SFH) in the two deep fields, finding that while currently quiescent, both regions experienced a substantial burst ~ 2 Gyr ago and a smaller burst ~ 500 Myr ago, which likely formed F8D1's nuclear star cluster. In the shallow fields, using the ratio of evolved Asymptotic Giant Branch and Red Giant Branch stars out to ~ 13 kpc along F8D1's known stellar stream, we confirm that F8D1 was globally star-forming until at least 2 Gyr ago. We estimate a total progenitor stellar mass, including the stream, of $\sim 1.3 \times 10^8 M_{\odot}$, with an average $[M/H] \sim -0.8$. We compare F8D1's properties to those of Local Group galaxies with similar initial stellar mass. We find that F8D1 is consistent with a progenitor star-forming galaxy similar to NGC 6822, which is in the midst of a transition to a Sagittarius-like system. Notably, this evolutionary sequence can be accomplished through tidal processing alone, in galaxies that have experienced sufficiently bursty feedback to create cored profiles.

1. INTRODUCTION

1.1. Ultra Diffuse Galaxies: Extreme End of the LSB Population

In the last decade, a newly-labeled class of low surface brightness (LSB) galaxy has been discovered

* Hubble Fellow

in unexpectedly large numbers in both nearby galaxy clusters and throughout the local field: so-called ultra-diffuse galaxies (UDGs; van Dokkum et al. 2015a; Koda et al. 2015; Mihos et al. 2015). Though LSB galaxies have been studied for decades (with their own rich literature, e.g., Dalcanton et al. 1997; de Blok & McGaugh 1997, and others), and there is no ironclad set of UDG selection criteria, these UDGs have rapidly garnered intense interest owing to their extreme properties, including relatively low stellar masses ($M_{\star} = 10^7 - 10^{8.5} M_{\odot}$), yet radii ($R_{\text{eff}} = 2 - 4 \text{ kpc}$) rivaling much more massive galaxies, and extremely faint central surface brightness (SB; $\mu_{0,V} \gtrsim 23 - 24 \text{ mag arcsec}^{-2}$). The discovery of these galaxies has challenged the field to account for their existence in the standard paradigm of galaxy formation. Do these galaxies follow unique evolutionary channels, or are they an expected edge case of the overall galaxy distribution?

Extreme examples of these UDGs have been discovered in the Local Group (e.g., the Sagittarius dwarf galaxy, Ibata et al. 1995; Andromeda XIX, McConnachie et al. 2008; Antlia 2, Torrealba et al. 2019); the faintest of which were effectively hidden prior to the discerning power of nearby stellar motions provided by *Gaia*. Evidence suggests that these Local Group UDGs are exclusively in the final throes of tidal disruption. It is unclear whether these nearby systems are analogous to the emerging populations of more distant UDGs, which are, in contrast, largely symmetric and exhibit no discernible evidence of disruption to deep SB limits (van Dokkum et al. 2015b; Burkert 2017; Lim et al. 2020). Furthermore, many UDGs have been found in the field, far from the tidal influence of a massive central galaxy (Papastergis et al. 2017; Barbosa et al. 2020). With the discovery of enigmatically rich globular cluster populations in some (but not all) UDGs (e.g., Peng & Lim 2016; van Dokkum et al. 2016; Amorisco et al. 2018; Lim et al. 2020), unusual inferred mass-to-light ratios in several systems (e.g., van Dokkum et al. 2018; Toloba et al. 2018; Danieli et al. 2019; van Dokkum et al. 2019; Toloba et al. 2023), and high neutral gas fractions in the field (e.g., Papastergis et al. 2017; Mancera Piña et al. 2019; Jones et al. 2023), the mystery of UDGs has only deepened. How do these unique galaxies form?

Like their observational properties, a theoretical consensus on the origins of UDGs has yet to be reached. Four primary ideas have emerged from theoretical studies: (1) tidal processing in cluster or group environments (Yozin & Bekki 2015; Safarzadeh & Scannapieco 2017; Carleton et al. 2019), (2) unusually bursty star formation histories (SFHs), resulting in stellar feedback-driven oscillation of galaxy sizes (El-Badry et al. 2016;

Di Cintio et al. 2017; Chan et al. 2018), (3) early accretion of gas with high angular momentum, resulting in a naturally shallower central potential and more diffuse star formation for a high-spin tail of normal galaxies (Amorisco & Loeb 2016), and (4) ‘failed’ galaxies, who experienced violent early star-forming episodes that completely expelled their gas reservoirs before they could form a dense baryonic component (van Dokkum et al. 2015a; Peng & Lim 2016; Ferré-Mateu et al. 2023; Toloba et al. 2023). Some of these mechanisms are mutually exclusive, yet particularly for UDGs in cluster or group environments, most of these mechanisms could work in concert. Further complicating this picture, how UDGs are observationally defined plays an important role in pinning down distinct physical origins (e.g., Van Nest et al. 2022), as with any unusual galaxy population.

It is clear that no single galaxy will encompass all of the unusual properties of the UDG population. However, thus far only the UDGs in the Local Group have been studied to the level of their individual resolved stellar populations (e.g., And XIX; Collins et al. 2022). The flavor of evidence is therefore very different when comparing Local Group UDGs to their more distant counterparts. An equally in-depth study of a UDG at intermediate distance, in a different group environment, would go a long way to helping improve understanding of the evolutionary trajectories of these exceptional galaxies. Enter: F8D1.

1.2. F8D1: A Prototypical UDG

F8D1, discovered by Caldwell et al. (1998) in a CCD survey with the Burrell Schmidt telescope on Kitt Peak and confirmed with the *Hubble Space Telescope* (*HST*), is a nearby low-surface brightness dwarf galaxy at the distance of the M81 Group (M81 TRGB distance is 3.6 Mpc, Radburn-Smith et al. 2011; F8D1 TRGB distance is 3.8 Mpc, Weisz et al. 2008). We give a visual summary of the M81 Group in Figure 1, showing the positions of the major galaxies overlayed on the density of RGB stars detected in Subaru Hyper Suprime-Cam (HSC) imaging, using data presented in Smorcina et al. (2020), Žemaitis et al. (2023), and new observations from the recent Subaru/Gemini exchange proposal S23A-TE088-GQ (PI: Bell).

Nearly invisible in typical ground-based imaging, such as SDSS, F8D1 is the lowest surface brightness ($\mu_{V,0} \simeq 25 \text{ mag arcsec}^{-2}$; Caldwell et al. 1998) known satellite of the M81 Group of galaxies. The M81 Group is a rich environment, with three satellites at least as massive as the LMC: the starburst disk galaxy M82, the compact elliptical NGC 3077, and the M33-analog flocculent spiral NGC 2976. Both M82 and NGC 3077 ap-

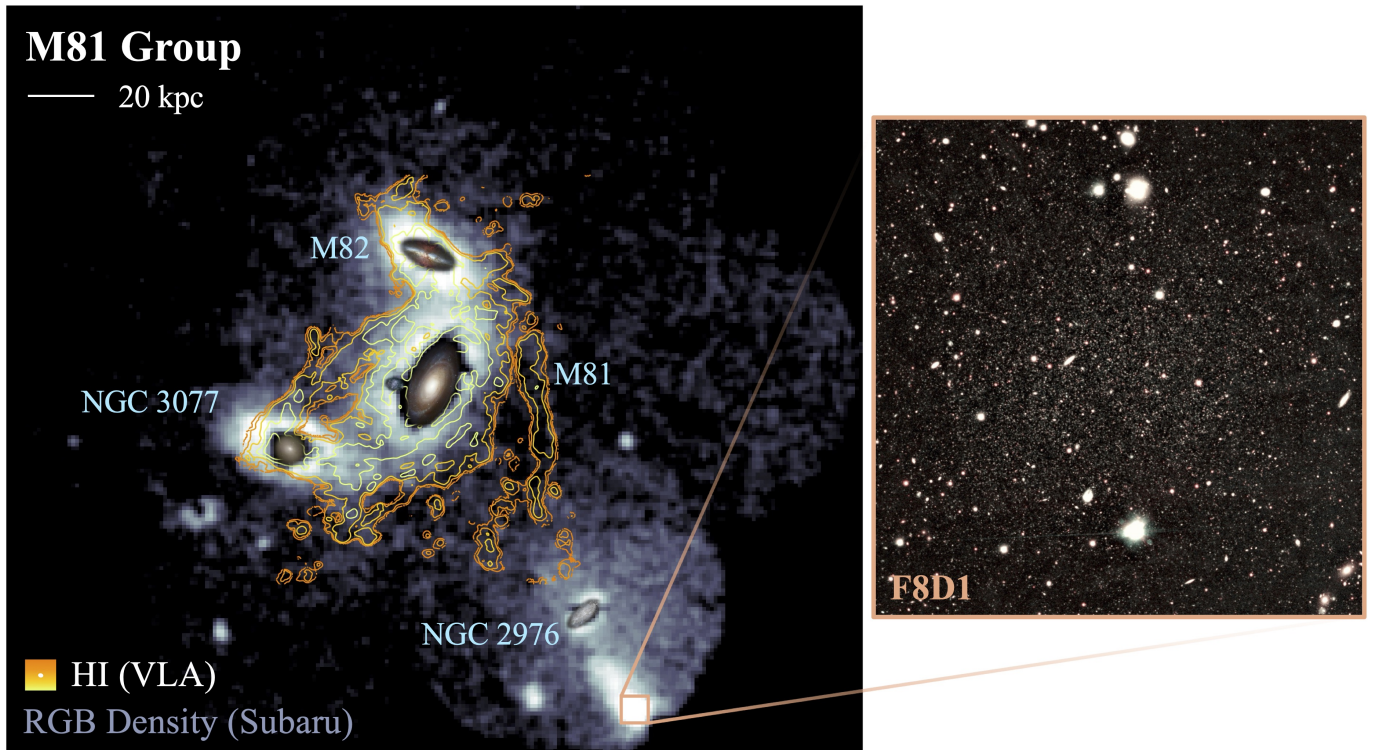


Figure 1. Density of RGB stars in the M81 Group, revealing the global structure of its stellar halo and providing group context for F8D1 (lower right) and its extended tidal stream. North is up and East is left. RGB stars have been selected according to the [Smercina et al. \(2020\)](#) criteria for *gri* photometry, including size $< 0''.7$, colors consistent with the $g-r/r-i$ stellar locus, and within 1.8 magnitudes of the tip of the RGB. The density map features $1''.1$ pixels, smoothed with a $\sigma = 0.8$ pixel Gaussian kernel, and is scaled logarithmically (minimum value of 1, maximum value of 25). Stars were detected and identified in multi-epoch three-filter Subaru HSC imaging. Also overlaid are contours of H I 21 cm emission, from the [de Blok et al. \(2018\)](#) natural-weighted D-array VLA Moment 0 map. Contours are shown in logarithmic steps of 0.5 from 0.01–3 Jy beam km s^{-1} . The VLA beam is shown as the white filled ellipse at the bottom left. A zoomed *r/i* Subaru HSC color-image of F8D1 is shown in the right panel.

pear to be in an advanced gravitational interaction with M81 ([Yun et al. 1994](#); [Okamoto et al. 2015](#); [Smercina et al. 2020](#)), while NGC 2976 may or may not have yet experienced a close pass to M81 ([Williams et al. 2010](#); [Drzazga et al. 2016](#)). F8D1 is ~ 120 kpc to M81’s south-west (in projection) — much nearer to NGC 2976 in projected distance.

We show the properties of F8D1 in the context of other galaxy populations in Figure 2, including “normal” galaxies from the CALIFA survey²⁰ ([Méndez-Abreu et al. 2017](#)), Local Group dwarf galaxies ([McConnachie 2012](#)), and known UDGs at larger distances, both in the Coma Cluster ([van Dokkum et al. 2015a](#); [Yagi et al. 2016](#)) and near known groups/associations in low-density environments ([Merritt et al. 2016](#); [Marleau et al. 2021](#)). This is not an exhaustive compari-

son, and selection functions of the comparison samples have not been considered. Figure 2 is simply illustrative of the unique properties of UDGs among other galaxy populations and shows that, indeed, F8D1 is prototypical among known UDGs. This makes F8D1 the nearest ‘garden variety’ UDG that has been resolved into its constituent stars.

As is readily apparent in Figure 1, access to its stellar populations on large scales has revealed an extended tidal stream associated with F8D1, first described by [Žemaitis et al. \(2023\)](#). In order to disentangle the role of the various UDG formation scenarios in F8D1’s evolution, we obtained deep HST imaging of its center and extended stream, and of a number of additional flanking fields along the stream. We present the results of this survey in the remainder of this paper. We describe the data in §2, including the observations (§2.1) and stellar photometry (§2.2), followed by our results in §3. In §3.1, and its subsections, we describe the process of fitting observed color–magnitude diagrams (CMDs) of F8D1’s stars to reconstruct its star formation

²⁰ The CALIFA sample are relatively nearby galaxies, with morphological types spanning the Hubble Diagram, masses $M_* > 10^9 M_\odot$, and a median distance of 67 Mpc.

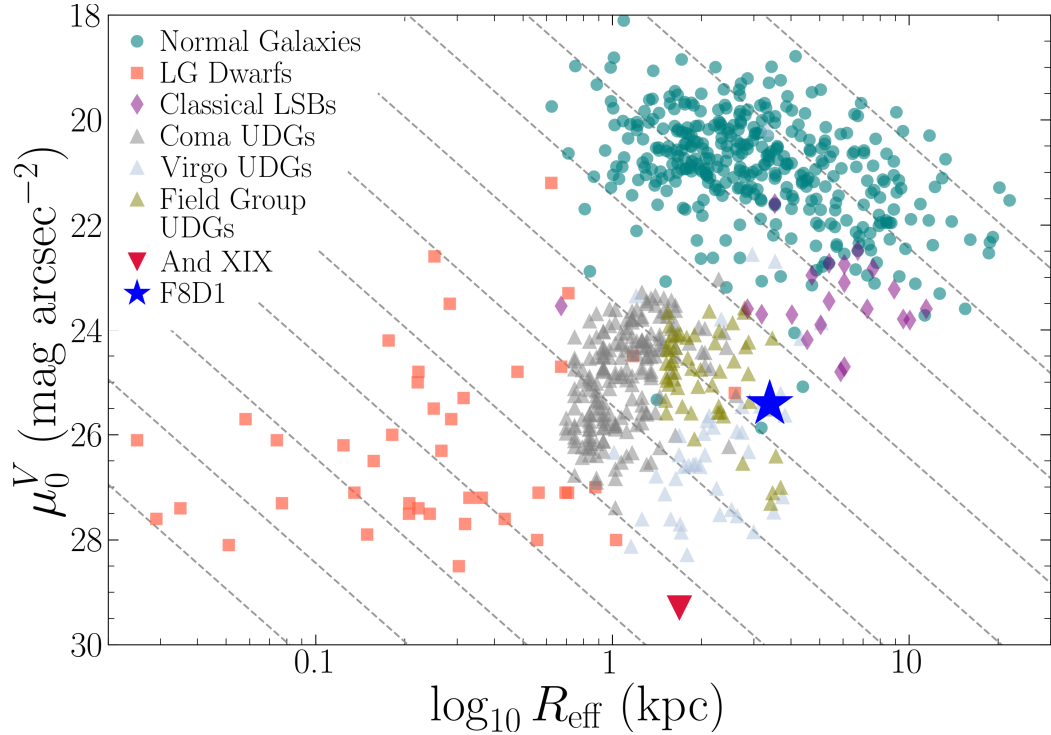


Figure 2. Effective (half-light) radius of different galaxy populations plotted against their central surface brightness in V-band (μ_0^V). Lines of constant absolute V-band magnitude (M_V), assuming an exponential surface brightness profile, are shown as gray dashed lines, ranging from -2 (lowest; faintest dwarf galaxies) to -22 (highest; brightest galaxies). “Normal” galaxies are taken from the CALIFA survey (Méndez-Abreu et al. 2017) and McGaugh (2005), shown as teal circles. Local Group dwarf galaxies are taken from McConnachie (2012) and are shown as red squares. Classical LSBs are taken from Dalcanton et al. (1997) and de Blok & McGaugh (1997), shown as purple diamonds. UDGs identified in the Coma Cluster are shown as gray triangles, taken from van Dokkum et al. (2015a) and Yagi et al. (2016). UDGs in the Virgo Cluster are shown as light blue triangles, taken from Lim et al. (2020), with $\mu_{0,V}$ provided via private communication by Sungsoo Lim, and radii calculated assuming a distance of 16.5 Mpc (Mei et al. 2007; Blakeslee et al. 2009). Several samples of UDGs discovered in galaxy groups in low-density environments are also shown as olive triangles, taken from Merritt et al. (2016) and Marleau et al. (2021). Andromeda XIX, the tidally disrupted extremely diffuse satellite of M31 (e.g., Collins et al. 2022), is denoted by a downward red triangle. Finally, F8D1 is denoted by the large blue star, using the original values measured by Caldwell et al. (1998). Note that we derive updated parameters for F8D1 in § 3.3.

history (SFH). In § 3.2, we present a larger-scale analysis of the “shutdown time” of star formation in F8D1 using the ratio of luminous AGB-to-RGB stars in the shallower flanking fields, and compare to the SFH fits. In § 3.3, we use the full HST dataset, in conjunction with ground-based archival data, to model the radial structure of F8D1 and estimate the total stellar content. § 4 contains a detailed discussion of F8D1’s evolution and its relevance to the evolution of other ultra-diffuse systems. We end with our conclusions in § 5.

2. DATA

2.1. Observations

The observations presented in this paper were taken through the Hubble Space Telescope Cycle 28 program GO-16191 (PI: Smercina). The observations were taken between 09 December 2020 and 21 February 2022. 19 of the 31 orbits were executed during the Cycle 28

schedule (late 2020–early 2021), the remaining 12 orbits were rescheduled to the following cycle due to single guide star acquisition failures during the initial visits.

We targeted the cataloged center of F8D1 with the Wide Field Camera 3 (WFC3), as well as coordinated parallel Advanced Camera for Surveys (ACS) observations for a field to the north east, for a total of 27 orbits. Each single-orbit visit was divided into three equal-length WFC3 sub-pixel dithers, using a linear 3-point pattern with $0''.135$ spacing, for a target of 2,715 seconds of total exposure time per orbit. Corresponding parallel observations comprised three *approximately* equal-length corresponding ACS exposures, for a target of 2,567 seconds of total exposure time per orbit. The visits were also manually mapped to a 4-point box pattern, achieved by using POS TARG to shift the target positions from visit-to-visit, designed to cover the chip gap. The box was designed with vertices $(-2.042, -2.173)$,

Table 1. Observations

Field Name	R.A. (hh:mm:ss)	Dec. (dd:mm:ss)	Camera	Filter	Date	Exp. (s)	50% Comp. (mag)
NAME-F8D1	09:44:46.6	+67:26:18.9	WFC3	F814W	2021-01-31	46,059	28.34
				F606W	2021-02-01	27,108	28.77
F8D1-257ne-35908	09:45:30.1	+67:30:17.9	ACS	F814W	2021-02-01	33,281	28.37
				F606W	2021-01-31	33,301	29.07
F8D1-FIELD1	09:44:55.3	+67:29:40.2	WFC3	F814W	2021-02-06	1,392	...
				F606W	2021-02-06	1,200	...
F8D1-FIELD2	09:45:07.3	+67:31:54.3	WFC3	F814W	2021-02-05	1,392	...
				F606W	2021-02-05	1,200	...
F8D1-FIELD3	09:45:34.8	+67:22:22.0	WFC3	F814W	2022-02-11	1,392	...
				F606W	2022-02-11	1,200	...
F8D1-FIELD4	09:45:10.8	+67:23:43.1	WFC3	F814W	2020-12-09	1,392	...
				F606W	2020-12-09	1,200	...
F8D1-419ne-34689	09:45:29.1	+67:34:26.6	ACS	F814W	2021-02-06	1,153	...
				F606W	2021-02-06	1,103	...
F8D1-566ne-34999	09:45:43.9	+67:36:29.8	ACS	F814W	2021-02-05	1,153	...
				F606W	2021-02-05	1,103	...
F8D1-448se-34499	09:46:06.8	+67:27:14.8	ACS	F814W	2022-02-11	1,165	...
				F606W	2022-02-11	1,115	...
F8D1-632se-7787	09:45:59.8	+67:20:24.4	ACS	F814W	2020-12-09	1,153	...
				F606W	2020-12-09	1,103	...

NOTE—Summary of observations, including coordinates, camera, filter, and exposure information. Deep fields are listed first, followed by the shallower flanking fields. In each case, the ACS parallels that correspond to each WFC3 primary observation are ordered the same as their WFC3 counterparts. For example, F8D1-FIELD1 and F8D1-419ne-34689 were taken in parallel. For the deep fields, we also give the 50% completeness depth in each camera, determined from ASTs (§ 2.2). See § 2 for a more detailed description of the observations.

(2.042, -2.173), (2.042, 2.173), (-2.042 , 2.173); each four visits therefore completed a full box pattern. Of the 27 orbits, the WFC3 observations were divided into 17 orbits for the F814W filter and 10 orbits for the F606W filter, while the ACS observations were divided into 14 orbits for F814W and 13 orbits for F606W. We designed this observing strategy to detect resolved individual stars at the distance of F8D1 to approximately one magnitude below the predicted core helium-burning phase for old stellar populations, the ‘Red Clump’ (RC; [Alves & Sarajedini 1999](#); [Girardi 2016](#)), in both cameras.

We also targeted four single-orbit “flanking” fields with WFC3 as primary and coordinated ACS parallels, aimed at detecting the presence of possible tidal debris or extended stellar outskirts in F8D1. Each of these four flanking fields was observed in both F606W and F814W, with two dithered exposures each. To maximize the exposure time possible in a single orbit, we split the total F606W exposure time per orbit by $\sim 1/3$ in the first exposure and $\sim 2/3$ in the second, and the opposite for F814W ($\sim 2/3$ and $\sim 1/3$, respectively). Ex-

ecuted exposure times sometimes varied by several seconds relative to the Phase-II program submitted in the Astronomer’s Proposal Tool (APT), particularly for the rescheduled observations, to adjust for HST’s evolving orbital visibility window. The total executed exposure times for each field in this program are given in Table 1. All images can be obtained from the MAST archive: [doi:10.17909/zry4-hr90](https://doi.org/10.17909/zry4-hr90).

2.2. Photometry

We performed point spread function (PSF)-fitting on the HST pipeline-calibrated images (f1c extension) using the most up-to-date version of the DOLPHOT software package ([Dolphin 2000, 2016](#)). We ran artificial star tests (ASTs) in the two deep fields to assess the photometric quality, completeness, and bias of our observations. For each field, we used the Bayesian Extinction and Stellar Tool (BEAST) package ([Gordon et al. 2016](#)) to generate input lists of 170,000 artificial stars, sampled from a realistic range of stellar population models. We then used DOLPHOT to run these input lists as ASTs, following the method developed by the Panchro-

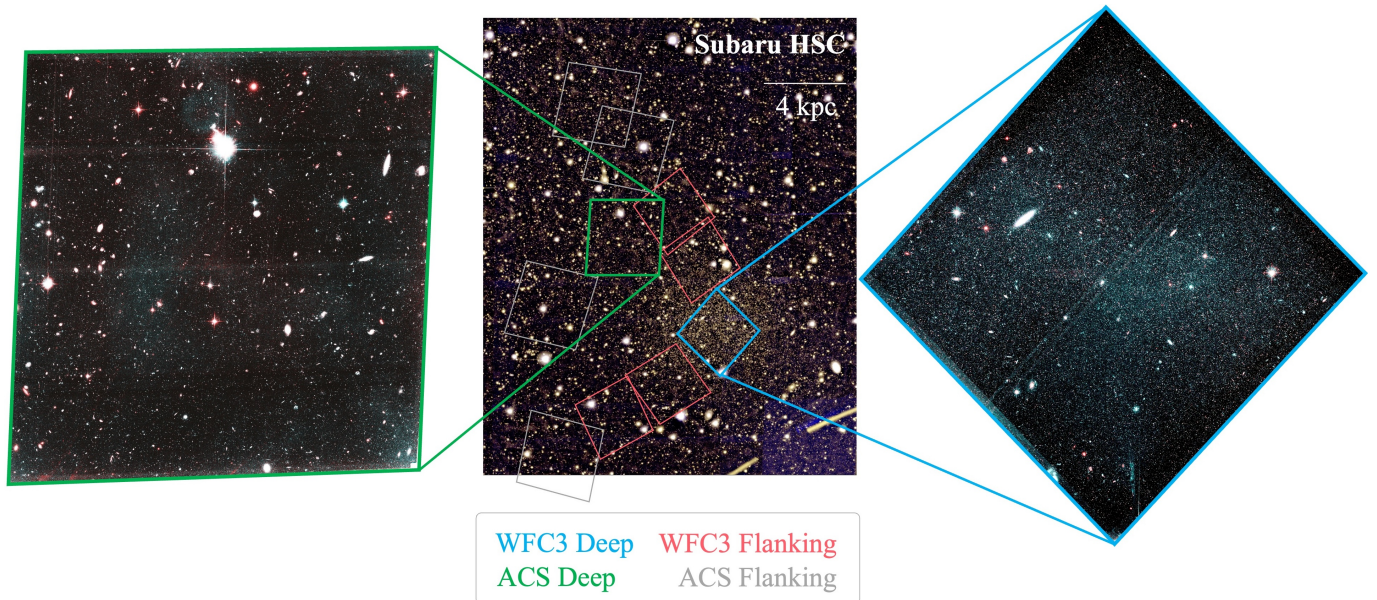


Figure 3. Overview of the layout of our HST survey of F8D1, with a g,r,i image from Subaru HSC at the center. The two deep fields are shown, with WFC3 in blue and ACS in green, as well as the shallower flanking fields, with WFC3 pointings in red and ACS in gray. We also show the drizzled F606W/F814W images for the two deep fields as zoomed insets. Images are oriented with North up and East to the left. The central WFC3 field covers F8D1’s approximate effective radius.

matic Hubble Andromeda Treasury (PHAT) program (Williams *et al.* 2014).

Using the results of the ASTs, we compute completeness curves in each filter, for each target field. We used these completeness curves to optimize the selection criteria for stellar sources — i.e. balancing loosening criteria for greater depth and tightening them to reduce contamination. We consider sources to be ‘good stars’ (GST), if they pass our criteria for DOLPHOT’s signal-to-noise ratio (SNR), crowding (CROWD), and sharpness (SHARP) parameter outputs. Due to the depth of our imaging, and very little foreground or background contamination, we choose slightly lower SNR criteria than are typically used in the deep fields. In depth-limited, rather than crowding-limited, fields such as these the CROWD parameter is particularly useful for identifying spurious sources; for example, the diffraction spikes of bright foreground stars, which are often resolved into many individual sources. In all fields, we choose the smallest CROWD parameter that is able to remove the majority of these contaminating sources without significantly changing the measured 50% completeness depth relative to more standard values, such as used by the PHAT Survey. For example, adopting the CROWD and SHARP values of (Williams *et al.* 2014) yields changes of <0.05 mag to our completeness limits, for the same SNR. We give our GST criteria for each field and camera combination in Table 2.

In Figure 4, we show photometry residuals and the completeness curves for GST sources in F606W and

F814W, for the deep WFC3 and ACS fields. In Figure 5, we show the GST color–magnitude diagrams (CMDs) and density maps for the two deep fields. These observations are very deep, with 50% completeness limits of 28.77 in F606W and 28.34 in F814W for WFC3, and 29.07 in F606W and 28.37 in F814W for ACS.

3. RESULTS

In the following sections, we present the results of our analysis of these observations. First, in § 3.1 we fit our photometry to infer detailed star formation histories (SFHs) over the past 6 Gyr for both of the central WFC3 and outer ACS deep fields in F8D1. Next, in § 3.2 we use the ratio of the number of luminous Asymptotic Giant Branch (AGB) stars to stars on the upper Red Giant Branch (RGB) to estimate the ‘quenching time’ for star formation across F8D1, and compare these results to the full calculated SFHs. Finally, we use these and other results from the literature to study the structure of F8D1 using resolved star counts.

3.1. A Detailed History of Star Formation in F8D1

Our observations in the deep WFC3 and ACS fields reach ~ 1.0 mag below the RC at high photometric completeness, providing reliable access to F8D1’s ancient stellar populations and SFH. To calculate the SFHs of these populations, we use the well-tested color–magnitude fitting software MATCH (Dolphin 2002). Using stellar evolutionary models, MATCH forward models the observed CMD of a stellar population as a com-

Table 2. GST Selection Criteria

Field+Camera	$\text{SNR}_{\text{F606W}}$ (>)	$\text{SHARP}_{\text{F606W}}^2$ (<)	$\text{CROWD}_{\text{F606W}}$ (<)	$\text{SNR}_{\text{F814W}}$ (>)	$\text{SHARP}_{\text{F814W}}^2$ (<)	$\text{CROWD}_{\text{F814W}}$ (<)
Deep WFC3	3.3	0.1	1	3.3	0.1	1
Deep ACS	3.3	0.3	0.2	3.3	0.3	0.2
Shallow WFC3	4	0.1	0.2	4	0.1	0.2
Shallow ACS	4	0.1	0.2	4	0.1	0.2

NOTE—Selection criteria for ‘Good Star’ (GST) sources, using the DOLPHOT output parameters.

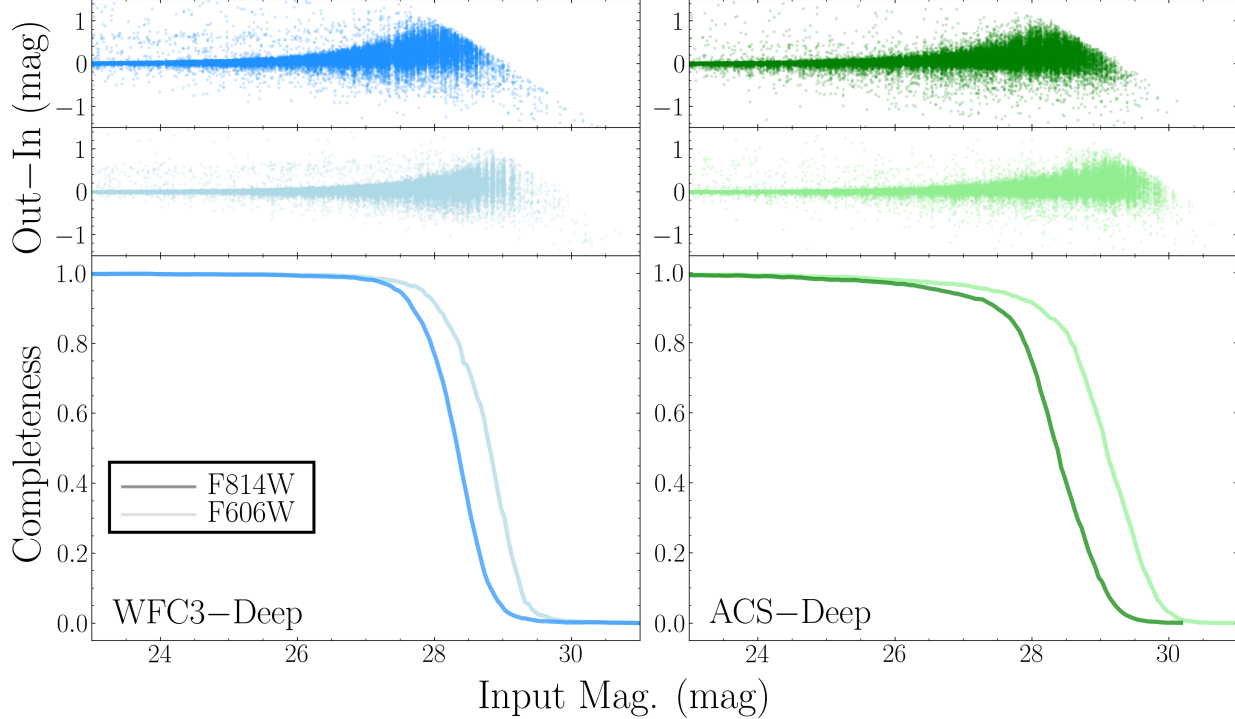


Figure 4. Summary of the data quality in the two WFC3 (left column; blue) and ACS (right column; green) deep fields, for GST sources selected in F8D1, assessed from the AST results. Results for the F606W filter are shown in the lighter shade, and those for F814W in the darker shade. The top two rows show the difference in the measured magnitudes of GST-selected artificial stars compared to their input magnitudes. As is commonly seen near the completeness limit, there is a slight bias for the faintest stars, where they are measured to be 0.1–0.2 magnitudes fainter than expected on average. This suggests the data are not crowding-limited, as blends in crowded fields would typically show biases to brighter recovered magnitudes. The bottom row shows the detection completeness of recovered artificial GST-selected sources, as a function of magnitude.

posite of stars formed at different ages and with different metallicities (see Weisz et al. 2014 for an updated description). It is a widely used tool for deriving the SFHs of stellar populations in dwarf galaxies throughout the local universe (e.g., Weisz et al. 2008; McQuinn et al. 2009, 2010; Weisz et al. 2011, 2012, 2014; McQuinn et al. 2015; Albers et al. 2019; Gallart et al. 2021; Rusakov et al. 2021; Collins et al. 2022; McQuinn et al. 2023; Savino et al. 2023, and others). When comparing the results of observations reaching below the RC and much deeper observations reaching the oldest main sequence turnoff (oMSTO), Weisz et al. (2014) found that

photometry resolving the RC is sufficient for MATCH to recover accurate SFHs back to ~ 6 Gyr.

We use the Padova stellar libraries (Girardi et al. 2000; Cioni et al. 2006; Marigo et al. 2008; Girardi et al. 2010; Girardi 2016) to fit the deep CMDs of F8D1’s stellar populations and calculate their SFHs. The updated Padova model suite (distinct from the related PARSEC suite; Bressan et al. 2012) supports a broad range of metallicities, and includes model tracks for thermally-pulsating (TP)-AGB stars, of which F8D1 appears to have a substantial population. We fit the SFH using 71 logarithmically-spaced time bins, with bin size

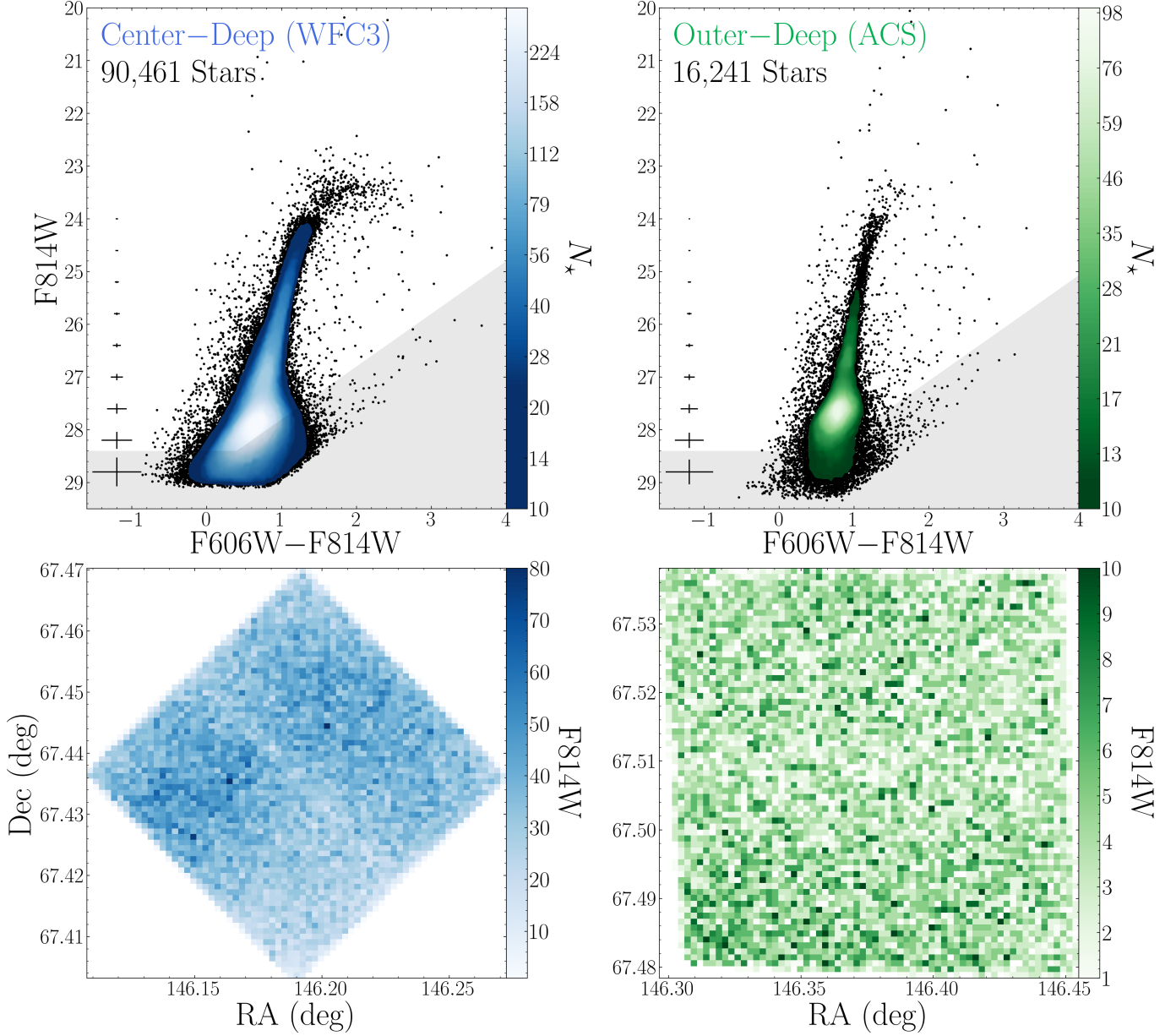


Figure 5. *Top row:* Color-magnitude diagrams (CMDs) of GST-selected stars in the central deep WFC3 field (left) and outer deep ACS field (right). Stellar density is shown above a level of $\sim 3,000 \text{ } \star/\text{mag}^2$ ($N_* = 10/\text{bin}$). Below this density individual stars are shown. Median errors for the photometry are shown to the left, from F814W = 24–29 mag at 0.6 mag increments. The Red Clump is visible above the 50% completeness curve (shown as shaded gray region) in both fields, with a center at F814W ~ 27.6 –27.8. As shown in Figure 7, the variable morphology of this feature encodes important information about F8D1’s SFH. *Bottom row:* Spatial density of GST sources in each field, shown at a scale of $\sim 3''$ per pixel.

0.05, from $\log[\text{Age (yr)}] = 6.6$ –10.15. We fit each field in *MATCH* assuming a Kroupa (2001) initial mass function, a binary fraction of 35% (the default for *MATCH*), and a fixed distance modulus of 27.9. Using our 71 time bins, we fit our observed CMDs with a grid of models with varying reddening. We assumed simple foreground reddening, as F8D1 does not host any detectable *in situ* ISM. We allowed for a range of foreground reddening values, as the Galactic cirrus in the vicinity of

the M81 Group is notably variable, from $A_V = 0.2$ –0.5 in steps of 0.05 mag. We find best-fit extinction values of $A_V = 0.25$ mag for the WFC3 field, and $A_V = 0.45$ mag for the ACS field.

We show the resulting SFHs in Figure 6, and the Hess Diagram model fits in Figure 8. Notably, both fields show strong bursts of star formation around 2–2.5 Gyr ago, with a sharp decline at 1–1.5 Gyr. Both fields also show a second distinct and statistically-

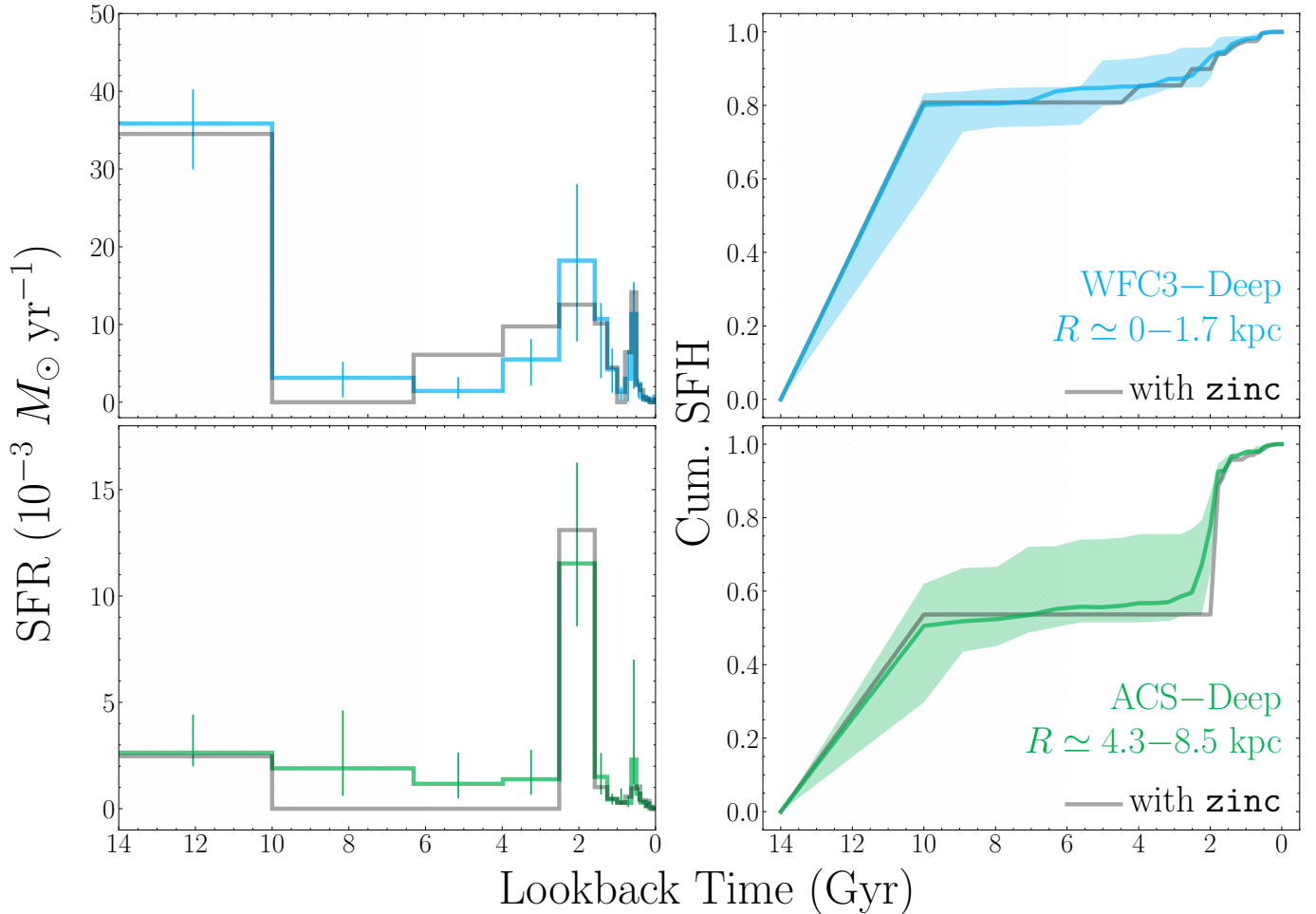


Figure 6. F8D1’s star formation history (SFH) calculated from the deep central WFC3 (top row, blue) and outer ACS (bottom row, green) fields. The instantaneous SFHs (SFR over time) are shown in the left column, while the cumulative SFHs, displayed as a fraction of the present-day stellar mass, are shown in the right column. The 1σ combined random and systematic uncertainties on the SFR in each bin are shown, and the corresponding 1σ envelopes for the cumulative SFHs are shown as shaded regions in the same color. Note the different y -axis scales for the two instantaneous SFHs. As discussed in §3.1.1, we show results for both a free age–metallicity relation (color) and a strictly increasing age–metallicity relation (MATCH’s **zinc** option; dark gray). The light hatched region denotes the age range where SFH results are highly uncertain for the photometric depth of these data. Note that these results correspond only to the FOVs shown in Figure 3.

significant burst of star formation ~ 500 Myr ago. In the central field, these bursts represent enhancements of $\sim 4\times$ and $\sim 3\times$ the lifetime average SFR, respectively. The burst at 2 Gyr in the outer field represented a $25\times$ enhancement over the average, while the 500 Myr burst was similar to the central field at $\sim 3\times$. The burst at 500 Myr formed a stellar mass of approximately $8\times 10^5 M_\odot$ within the central WFC3 field, of which $\sim 5\times 10^5 M_\odot$ remains. This burst coincides with the spectroscopic age estimate of F8D1’s nuclear star cluster (480 Myr; Forbes et al. 2024), which has a stellar mass of $\sim 3\times 10^4 M_\odot$ (Caldwell et al. 1998).

In Figure 7, we show comparison CMDs that exclude the 500 Myr and 2 Gyr bursts, but are otherwise equivalent to our best-fit model for the central deep

WFC3 field. It is visually apparent that the morphology of the observed CMD – particularly the bright-end of the RC and the AGB Bump, the populations blueward of the RGB, and the rich AGB population – cannot be well explained without these two periods of star formation enhancement.

In the following two sub-sections, we describe in greater detail our treatment of the age–metallicity degeneracy in the fits (§3.1.1), as well as the estimation of uncertainties on the fits (§3.1.2).

3.1.1. Age–Metallicity Relation

For our fiducial SFHs, we do not assume an age–metallicity relation, instead allowing the metallicity of stars formed in a given time bin to vary freely with age. This approach results in better fits to the observed

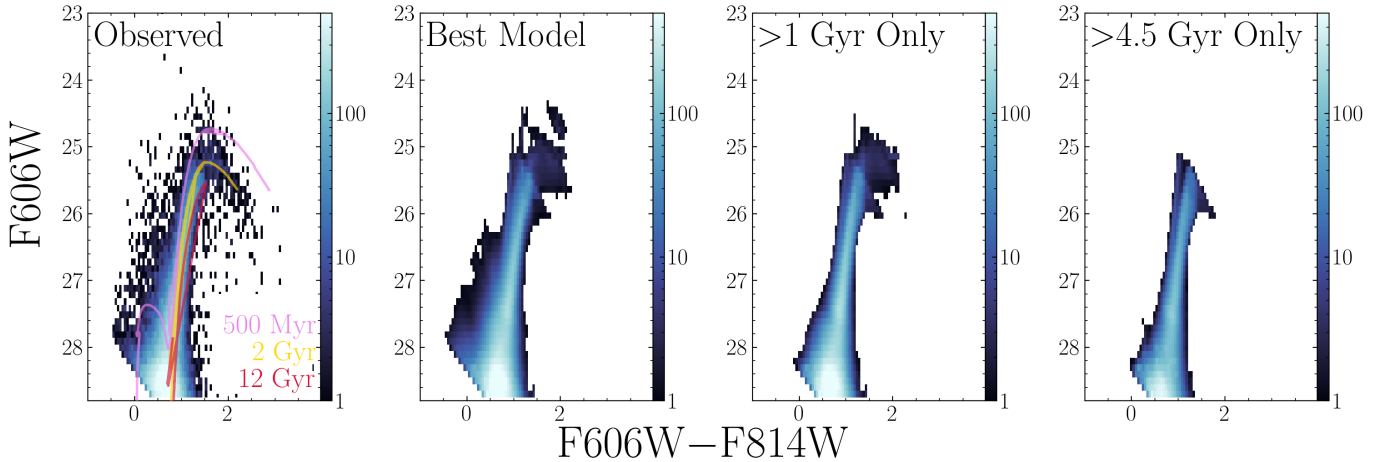


Figure 7. A comparison of the best-fit CMD model (second from left) of the central deep WFC3 data, to models with the 500 Myr (third from left) and 2–3 Gyr (right) bursts removed. We show the observed CMD (left) also for reference, with PARSEC isochrone tracks (Bressan et al. 2012) overlaid for the 500 Myr burst (pink; $[M/H] = -0.35$), 2 Gyr burst (gold; $[M/H] = -0.6$), and ancient population (red; $[M/H] = -0.85$). It is evident, particularly in the bright-end of the RC and the AGB Bump, the populations blueward of the RGB, and the rich AGB population, that the observed CMD can only be well modeled with the inclusion of the two recent bursts.

CMD, but introduces more degeneracy in the age–metallicity–reddening parameter space, and can sometimes produce unphysical metallicity values or changes over a galaxy’s lifetime. As the reddening in these fields is limited to the foreground cirrus, and it should be very common for the age–metallicity relation to be complex for all but the smallest galaxies, we forgo an assumption of an age–metallicity relation. We find that **MATCH** produces a reasonable age–metallicity relation in both fields, with an average change of $\lesssim 0.1$ dex between most adjacent time bins. For comparison, we also ran **MATCH** with a monotonically-increasing age–metallicity relation, as is often standard for dwarf galaxy SFHs (e.g., Weisz et al. 2014; Savino et al. 2023; McQuinn et al. 2024), using the **zinc** flag (i.e. ‘*Z* increasing’). In Figure 9 we show the resulting age–metallicity relation for our fiducial run, including the average over three broad age bins, and compare to the results from the **zinc** run. For the non-**zinc** run, we allowed $[M/H]$ between -2.3 and 0 . For the **zinc** run, we allowed -2.3 to 0 as the minimum/maximum initial metallicity, and -1.8 to 0 as the minimum/maximum present-day metallicity.

We see very good agreement in both fields between the average of the non-**zinc** and **zinc** runs, and observe an average metallicity increase of ~ 0.15 – 0.3 dex over from the oldest to youngest time bins. For the non-**zinc** runs, metallicity behavior appears fairly stable; bins with very low metallicities are typically insignificant to the overall fit, contributing $<1\%$ of the total stellar mass. There is one region of note: between 5–8 Gyr ago ($\sim 10^{9.7}$ – $10^{9.9}$ yr), there is a visible drop in metallicity in the central region, and a slight drop in the outer field at

the same ages. While the contribution to the total stellar mass formed in each field is negligible, which means there are few stars at that age present for constraining the metallicity, the consistent drop across fields, and across adjacent time bins within each field, could hint at a legitimate feature in the metallicity evolution of the galaxy. However, we also note that this is at the limit in age (5–6 Gyr) for which reasonable inferences of the SFH can be made (see § 3.1.2). A more accurate inference of F8D1’s age–metallicity relation will require deeper imaging or independent metallicity information (e.g., spectroscopy).

Overall, while allowing the metallicity in each time bin to be fit freely gives more room for physical variation in the metallicity evolution of the galaxy, the metallicity evolution for the significant star-forming bins reasonably reproduces a monotonically-increasing age–metallicity relation. Thus, the choice of an open or monotonically-increasing age–metallicity relation prior has no significant impact on the shape of F8D1’s SFH. While the remaining degeneracy in age and metallicity should preclude interpreting these age–metallicity relations as precise inferences, it is at least as accurate as the commonly used technique of estimating stellar metallicities from the color of the RGB. We therefore report the average metallicities in each field, for our fiducial SFH fit. For the central WFC3 field, the lifetime average metallicity is $[M/H] = -0.73$, with an average of $[M/H] = -0.53$ for star formation in the past 3 Gyr. The fit to the outer ACS field yields a slightly lower metallicity, with a lifetime average of $[M/H] = -0.84$, and an average of $[M/H] = -0.80$ for star formation in the past

3 Gyr. We note that this implies a remarkably flat radial metallicity gradient in F8D1.

3.1.2. SFH Uncertainties

The calculation of uncertainties in the inference of SFH from resolved CMD fitting is not trivial. The procedure for calculating both systematic uncertainties and statistical uncertainties with **MATCH** are described in detail in [Dolphin \(2012\)](#) and [Dolphin \(2013\)](#), respectively. We only provide a brief summary of these procedures here.

Statistical uncertainties are calculated using the **hybridMC** routine in **MATCH**, based on the Hybrid (or Hamiltonian) Monte Carlo (HMC) algorithm ([Duane et al. 1987](#)). **hybridMC** creates samples of SFHs, based on the fiducial fit, whose density is proportional to the probability density function. The 1σ spread around the weighted median is recorded.

Systematic uncertainties are more insidious, dominated by intrinsic variation in the calculation of stellar properties in different stellar model grids. Two approaches have been adopted: 1) directly fitting SFHs using multiple distinct model grids and comparing the results (e.g., [Williams et al. 2017](#); [Lazzarini et al. 2022](#); [McQuinn et al. 2024](#)); and 2) introducing random shifts in stellar parameters, designed to mimic the average empirical differences between large numbers of model suites (e.g., [Weisz et al. 2011](#); [Dolphin 2012](#); [Weisz et al. 2014](#)). See [Skillman et al. \(2017\)](#) for a direct comparison of each. Given the prominent populations of Thermally Pulsating AGB (TP-AGB) stars brighter than the tip of the RGB, and the relatively few model suites that accurately model this population, we opt for the latter method. We adopt depth-dependent values for shifts in $\log(T_{\text{eff}})$ (Effective Temperature) and M_{bol} (Bolometric Magnitude) following [Dolphin \(2012\)](#). Systematic uncertainties were estimated by running 50 Monte Carlo SFH fits, with each realization applying a single shift in $\log T_{\text{eff}}$ and M_{bol} for all stars, randomly drawn from normal distributions with $\sigma[\log(T_{\text{eff}})] = 0.022$ and $\sigma[M_{\text{bol}}] = 0.27$. We adopt the 68% range of these realizations around the median as our systematic uncertainty.

The statistical and systematic uncertainties are combined at the end of these steps (using the **MATCH** task **zcmerge**) into a single set of upper and lower 1σ uncertainty bounds on the SFH at each timestep. As is apparent in the SFHs shown in Figure 6, while the uncertainties on the SFR in each time bin may be significant, the corresponding uncertainties on the cumulative SFH, accounting for the covariance between time bins, is much better constrained. At the depth of our data (and with the numbers of stars detected), both the

Table 3. SFH Results

Cum. SFH (%)	τ_{WFC3} (Gyr)	τ_{ACS} (Gyr)
$M_{\star}^{\text{form}} =$	$5.19^{+0.58}_{-1.30} \times 10^7 M_{\odot}$	$5.82^{+0.46}_{-1.64} \times 10^6 M_{\odot}$
$\langle [M/H] \rangle_{\text{life}} =$	−0.81	−0.84
$\langle [M/H] \rangle_{3 \text{ Gyr}} =$	−0.53	−0.80
50	>6	>6
60	>6	$2.50^{+7.63}_{-0.28}$
70	>6	$2.17^{+5.24}_{-0.22}$
80	>6	$1.96^{+0.26}_{-0.10}$
90	$2.32^{+2.89}_{-0.42}$	$1.81^{+0.09}_{-0.18}$
100	$0.13^{+0.00}_{-0.07}$	$0.10^{+0.01}_{-0.04}$

NOTE—Results from the best-fit **MATCH** SFH. We give the look-back times (τ) at which fractions of the total stellar mass formed, from 50–100% in steps of 10%, for the WFC3 and ACS deep fields. We also give the total *formed* stellar mass,^a lifetime average metallicity, and average metallicity over the past 3 Gyr for the best fit in each field. Note that we estimate F8D1’s total *present-day* stellar mass to be $1.3 \times 10^8 M_{\odot}$ (see § 3.3). Times are not given for fractions <50%, as they are all at ancient times below the time sensitivity of our observations. A reminder that results for ages >6 Gyr are highly uncertain. Uncertainties at younger ages are typical of SFHs inferred for Local Group dwarfs.

^a**MATCH** calculates formed stellar mass by integrating from 0–100 M_{\odot} . Following [Telford et al. \(2020\)](#), we correct the masses reported by **MATCH** using a factor of 0.76 that brings these masses into agreement with a [Kroupa \(2001\)](#) IMF.

Table 4. AGB/RGB Ratio

Field	Radius (kpc)	$\log_{10} \left(\frac{\text{AGB}}{\text{RGB}} \right)$	τ_{90} (Gyr)
FIELD1	3.79	-0.92 ± 0.09	3.51 ± 1.62
419ne-34689	9.97	-0.93 ± 0.13	3.56 ± 1.63
566ne-34999	12.68	-0.76 ± 0.14	1.72 ± 1.50

NOTE—AGB/RGB ratios and corresponding τ_{90} for the three flanking fields used in this analysis (§ 3.2).

instantaneous and cumulative SFHs are well measured to ages of approximately 5–6 Gyr. At ages older than this, while difficult to fully account for in the systematic uncertainties, it has been well-documented that the age–metallicity degeneracy is essentially insurmountable without access to the oMSTO (e.g., [Weisz et al. 2014](#)).

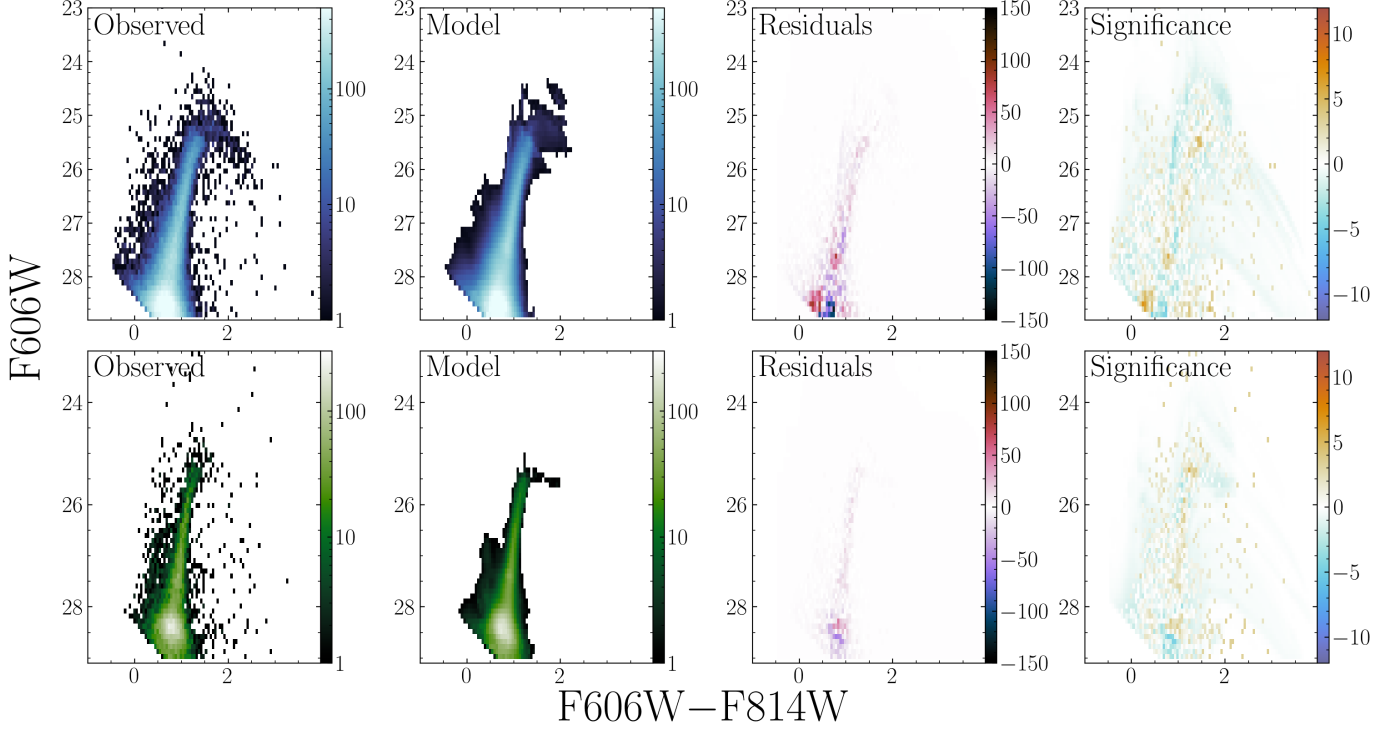


Figure 8. Hess Diagram fitting results for our fiducial SFH in the deep WFC3 (top row, blue) and ACS (bottom row, green). The leftmost column shows the observed Hess Diagram, the second column shows the best-fit model, the third column shows the raw residuals (data–model), and the fourth column shows the residual “significance” (the sum of the significance diagram returns the overall goodness-of-fit value). The residuals are largely unstructured in both cases, indicating good fits to the data.^a

^aNote that as the models draw from continuous tracks, some features with very low model densities (<0.1 star per pixel) are visible in the significance plots, such as the faint AGB ‘waterfall’ features extending to red colors.

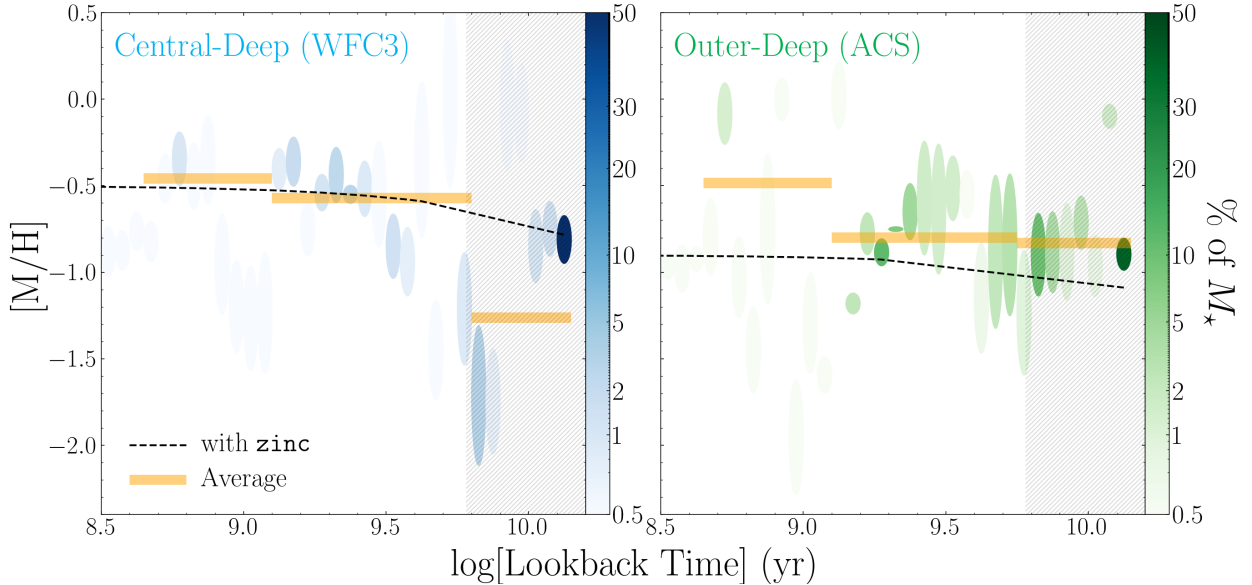


Figure 9. Recovered age–metallicity relations from MATCH for the two SFH fits to F8D1’s stellar populations. The axes of each ellipse denote the bin width (0.05 dex) and the combined uncertainty on $[M/H]$ for star formation within the bin. Ellipses are color-mapped to the fraction of total stellar mass formed in each. We have chosen a colormap that gives less visual weight to bins with a smaller contribution to the stellar mass. The average metallicity in three broad age bins is shown in orange. This is meant to illustrate the overall trends in the metallicity of the stellar populations over time. We note that the metallicity estimates that MATCH returns should not be taken as precise metallicity measurements (as can be inferred from the large uncertainty envelopes), but are useful as a rough guide. We also show the output when assuming the age–metallicity relation to be monotonically increasing (set using MATCH’s *zinc* argument). As in Figure 6, the most uncertain age range falls within the hatched region.

Readers should take this limitation into account when interpreting the age-metallicity and SFH fits.

We give results for the cumulative SFHs in Table 3, including the calculated lookback times at which the most recent 50% of the stellar mass formed.

3.2. Spatially Resolving the Quenching Time in F8D1 with Luminous AGB Stars

The photometry in the WFC3/ACS flanking fields is much shallower than the central deep fields, only reaching approximately 3 magnitudes below the TRGB, and shy of the RC. As such, they do not provide enough information to reliably overcome the age-metallicity degeneracy and reconstruct their SFHs as far back as 6 Gyr using MATCH. However, the populations of thermally-pulsating AGB (TP-AGB) stars brighter than the TRGB, as well as the most luminous populations of RGB stars, are both resolved at high-S/N. We show the CMDs of the flanking fields in Figure 10.

Harmsen et al. (2023) derived an empirical relation between the ratio of AGB-to-upper RGB stars and the time at which 90% of the stars formed in a population (τ_{90}), using SFHs derived from deep CMDs of quiescent Local Group dwarf satellite galaxies. The efficacy of this relation depends on the assumption that star formation is currently halted, and therefore that τ_{90} corresponds to the approximate ‘shutdown’ or ‘quenching’ time of star formation (e.g., Weisz et al. 2015; Skillman et al. 2017). Harmsen et al. (2023) found the following best-fit relation between the logarithm of the ratio between the number of TP-AGB to RGB stars and τ_{90} :

$$\tau_{90} = 4.4 \pm 0.3 \text{ Gyr} - 11.3 \pm 1.6 [\log_{10}(N_{\star, \text{AGB}}/N_{\star, \text{TRGB}}) + 1]. \quad (1)$$

AGB and RGB stars are selected from the CMD in 0.5 magnitude regions, identical to the Harmsen et al. (2023) selections, which are shown in Figure 10. The relation has an intrinsic scatter of 1.45 ± 0.18 Gyr, which in practice limits this technique’s usefulness to measuring $\gtrsim 1.5$ Gyr variations in τ_{90} .

The placement of the flanking fields relative to the 2 deep fields allows us to use this technique to estimate the quenching time of F8D1’s populations out to >10 kpc – well into the region visibly dominated by its stellar stream. Specifically, we use Field 2 ($R = 3.8$ kpc), Field 2-parallel (419ne-34689; $R \simeq 10$ kpc), and Field 4-parallel (566ne-34999; $R \simeq 12.7$ kpc), as they cover radii along F8D1’s stream axis that are distinct from the more precisely-measured deep fields. We use a set of eight fields from the GHOSTS survey, identified by Radburn-Smith et al. (2011) as containing only foreground stars and background galaxies, to correct for contaminant sources in these sparser flanking fields. We find that

both the AGB and RGB selection regions host, on average, 0.35 and 0.74 contaminants per ACS field (0.031 and 0.065 per arcmin²) using identical photometric cuts, with a scatter of 0.2. We give the ratios with Poisson and contaminant-subtraction uncertainties, as well as the estimated τ_{90} values with combined uncertainties, in Table 4.

Figure 11 shows the inferred τ_{90} as a function of radius. The three fields show fairly consistent ratios of ~ 0.12 – 0.17 , corresponding to τ_{90} s of 1.7–3.5 Gyr. These are consistent within the uncertainties with τ_{90} for the two deep fields of 2.3 Gyr and 1.79 Gyr (Table 3), suggesting that F8D1 was globally star-forming ~ 2 Gyr ago, with the inner regions of the galaxy and the outer regions currently contained in the tidal stream quenching relatively close to one another.

3.3. The Structure of F8D1 in Resolved Stars

Finally, we combined the deep fields and shallow flanking fields to investigate the radial structure of F8D1 and its stream. We selected stars from the top 2 magnitudes of the RGB (orange selection in Figure 10). To increase the number of data points for the radial profiles, we divided each HST field exactly in half. Uncertainties on the surface density of RGB stars in the flanking fields are the result of the quadrature sum of Poisson error and the uncertainty in the TRGB of each field due to differential extinction, at the level of ± 0.07 mag in $E(B-V)$. As in § 3.2, for the AGB/RGB analysis, we use the ‘empty’ fields identified by Radburn-Smith et al. (2011) to characterize foreground and background contamination. We find an average of 4.0 contaminants per ACS field (0.36 per arcmin²), using our photometric criteria and deeper RGB selection window, with a scatter of 0.9. We subtract this source density from all fields used in the density analysis.

We convert RGB density to stellar mass density by calibrating to the SFH fits for the two deep fields (§ 3.1; Table 3). It is important to note that MATCH calculates the *formed* stellar mass (which we correct to the equivalent for a Kroupa IMF; see Table 3 and Telford et al. 2020) and does not account for the mass lost by stellar death and evolved star winds. We correspondingly assume a 40% mass loss to present-day, consistent with a Kroupa (2001) IMF. Due to the age gradient between the two fields, we average the two fields to obtain a single conversion value of $5.23 \times 10^3 M_{\odot}$ per RGB star within our selection region. The uncertainty on this conversion factor is $\sim 11\%$ and includes the uncertainty on the total stellar mass formed in each field, and the Poisson error on the total number of stars in each of the two calibration fields. The total uncertainty on the stellar

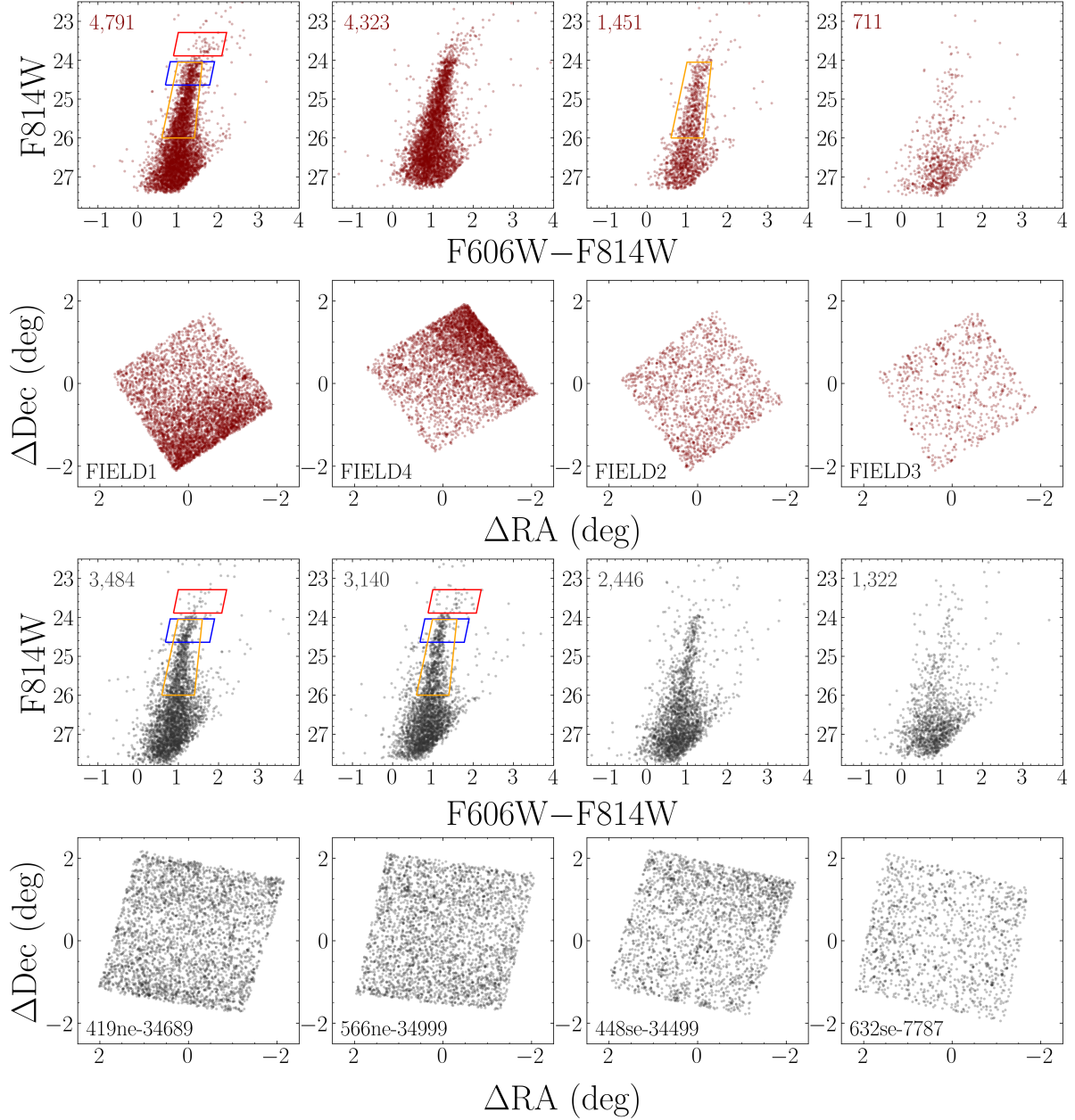


Figure 10. CMDs and maps of RGB-selected sources for our flanking fields. Following Figure 3, WFC3 fields are red and ACS fields are gray. Each camera is ordered by decreasing RGB density from left to right. We give the total number of stars in each CMD in the upper left corner. We show the selection regions used for AGB/RGB ratio as red and blue regions, each 0.5 magnitudes tall. We also show the RGB selection region for measuring F8D1’s density profile in orange, covering the brightest 2 magnitudes of the RGB. The unreddened TRGB is at $F814W \simeq 24.0$. Note that we do not calculate an AGB/RGB ratio for FIELD2, as it overlaps the ACS Deep field in radius. We do, however, use it in our density profile analysis.

mass surface density combines the uncertainty on the RGB surface density and stellar mass conversion.

Žemaitis *et al.* (2023) used star counts from Subaru HSC to detect and measure the profile of F8D1’s stream from ~ 9 –60 kpc. We combine these measurements with our HST measurements to provide a complete view of the galaxy from its center to 60 kpc along its stream, including a more accurate view of the in-

ner structure. One of the Žemaitis *et al.* (2023) data points overlaps with our HST field at 9 kpc. We scale this data point to match the value obtained for our HST data: their value of ~ 18 RGB stars arcmin $^{-2}$ at 9 kpc corresponds to an estimated stellar mass density of $3.54 \times 10^5 M_{\odot} \text{ kpc}^{-2}$ at the same radius in our HST field. We scale the remaining data points from Žemaitis *et al.* (2023) by the ratio of these two values.

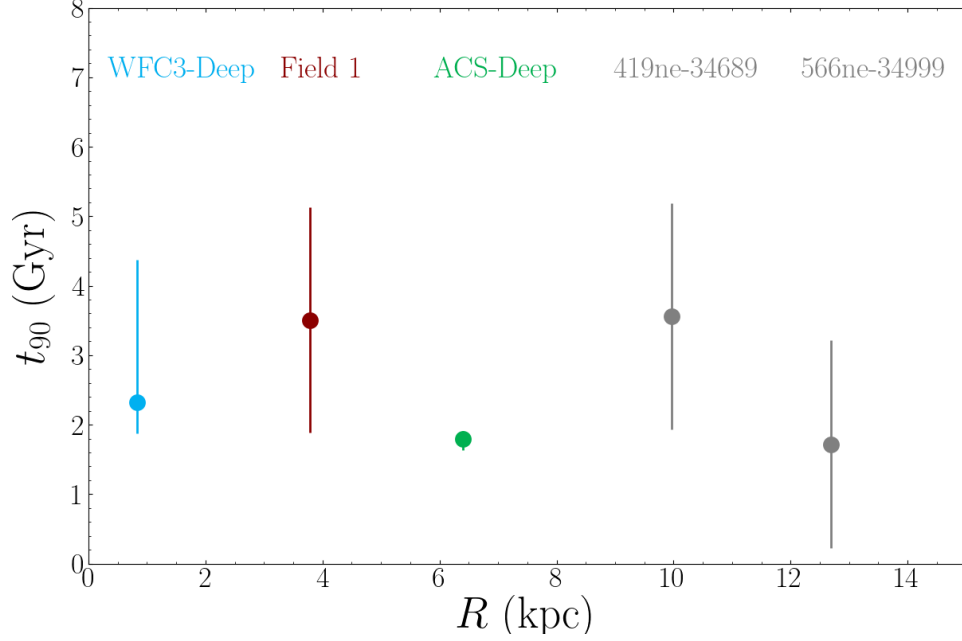


Figure 11. Radial profile of estimated τ_{90} (i.e. ‘quenching time’) in F8D1, in the direction of its tidal stream, combining our deep SFH analysis and inferences from the AGB-to-RGB ratio in several of the flanking fields. While individual points have substantial uncertainties, a universal quenching time within the past 3 Gyr, for the entire galaxy, appears to be a good fit to the data.

In the remainder of this section, we analyze the radial stellar mass surface density of F8D1 along the northern stream direction. Only northern half of the inner deep WFC3 field is considered as well as the remaining field halves from the ACS deep field and 4 WFC3+ACS flanking fields, and the 7 scaled points from Žemaitis et al. (2023). The profile appears to be well described by two components: 1) an inner component, which dominates at radii < 5 kpc; and 2) an outer component, which results in a dramatic flattening of the density profile and dominates at radii > 5 kpc. To physically describe this profile, we apply a two component Sérsic fit (Sérsic 1968) using the Python Markov Chain Monte Carlo (MCMC) fitting module `emcee`. We allow each Sérsic component to vary freely, parameterized using the half-light radius, R_e , as

$$I(r) = I_e \exp \left\{ -b_n \left[\left(\frac{R}{R_e} \right)^{1/n} - 1 \right] \right\}, \quad (2)$$

where n is the Sérsic index and b_n is the inverse of the regularized lower half incomplete gamma function, such that the incomplete gamma function (γ) and the complete gamma function (Γ) are related by $\Gamma(2n) = 2\gamma(2n; b_n)$.²¹ We adopt the log-likelihood func-

tion of Hogg et al. (2010) for a linear model fit to data:

$$\ln \mathcal{L} = -\frac{1}{2} \sum_{i=1}^n \left[\frac{1}{\sigma_i^2} (x_i - x'_i)^2 + \ln \sigma_{x,i}^2 \right], \quad (3)$$

where x_i is the data, x'_i is the model, and $\sigma_{x,i}$ is the uncertainty on each point. 5,000 realizations, with a discarded burn-in set of 200, was more than sufficient to obtain stability in the posterior probability density functions for each of the 6 parameters, which are shown in Figure 12. We show the radial profile, along with the best-fit components in Figure 13.

We integrate the two components to obtain estimates of the stellar mass in each. We assume the central component of F8D1 to be spherical. In this case, the second component, which we attribute to the stream, can be modeled as an ellipse with a semi-major axis in the stream direction and a semi-minor axis (i.e. width) equivalent to the effective radius of the inner component, where the two components meet. This gives us an approximate axis ratio for the stream of $b/a = R_{e,1}/R_{e,2}$, which we use to integrate the radial profile of the stream as an ellipse. We estimate uncertainties on the stellar mass of each component by integrating all 5,000 of the MCMC realizations and taking the corresponding 16–84% range. We estimate total stellar masses of $9.93^{+1.63}_{-1.40} \times 10^7 M_\odot$ for the main galaxy and $3.42^{+0.31}_{-0.21} \times 10^7 M_\odot$ for the northern stream. We combine the two components to estimate a total *progenitor* stellar

²¹ This is accomplished using the SciPy special function `gammaincinv`.

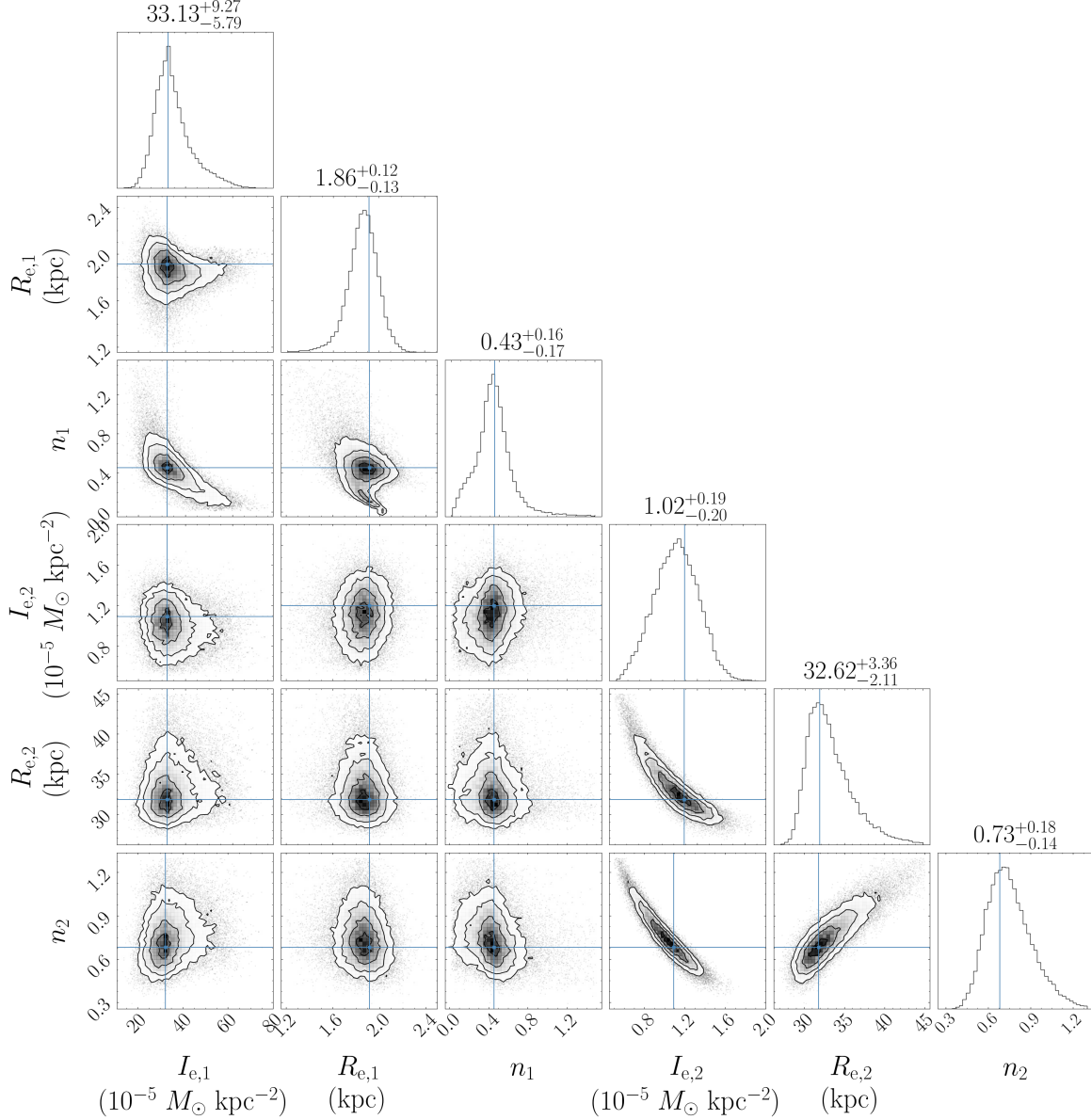


Figure 12. Corner plot showing the 1-dimensional and joint posterior probability distributions for the parameters in our two-component Sérsic model. See § 3.3 for details. Best-fit values are shown at the top of each column, corresponding to the parameter along the x -axis at the base of the column.

mass for F8D1 of $1.33^{+0.38}_{-0.14} \times 10^8 M_{\odot}$. This includes an additional uncertainty to the upper bound on F8D1’s total stellar mass, reflecting our complete uncertainty about the presence of a southern stellar stream component. Whether or not we expect a Southern component to the stream is entirely dependent on its orbital history (see § 4.1 for a more in-depth discussion); both are possible, for example if F8D1 is disrupting along a southwest path versus near a current apocenter, where the visible stream may comprise multiple distance components along the line-of-sight. We therefore add a 100% uncertainty (equal mass in the north and south) on the total mass of the stream component.

We give the parameters for the best-fit Sérsic models, as well as total stellar mass estimates in Table 5.

4. REFLECTIONS ON THE EVOLUTION OF F8D1 AND UDGS

In summary, our results indicate that F8D1 experienced multiple episodes of enhanced star formation: the first ~ 2 Gyr ago, followed by a period of sharp decline (i.e. initial ‘quenching’); the second, much smaller burst occurred only ~ 500 Myr ago, representing a brief period of rejuvenation that was followed by complete cessation of star formation to the present day (§ 3.1).

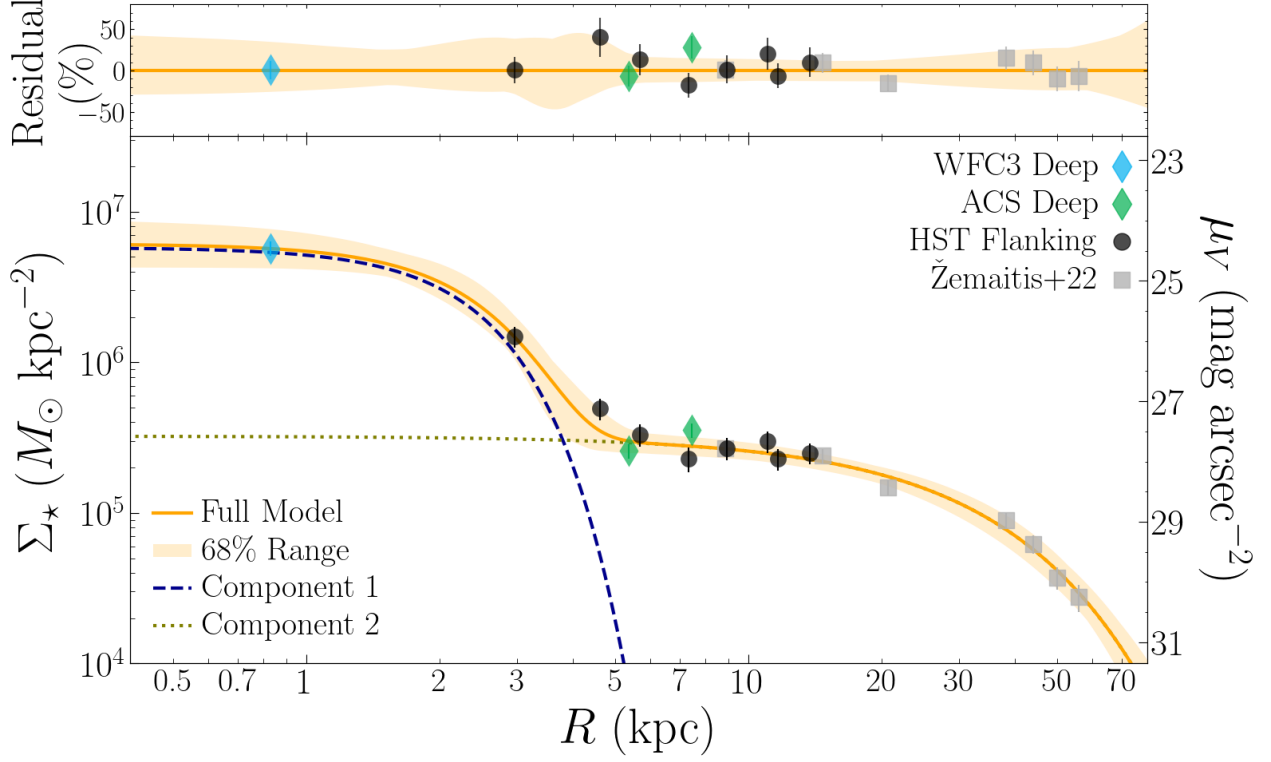


Figure 13. Radial stellar surface mass density, (Σ_*) profile of F8D1, calculated as described in § 3.3. Equivalent V -band surface brightness (μ_V) is shown on the right axis, assuming $M/L_V = 1$. The central and outer deep fields are shown as diamonds, colored blue and green, respectively. Only the northern half of the central WFC3 field is used, as we do not have extended radial coverage in the south at any other radii. All other HST fields are split into two equal-area measurements. The scaled measurements from Žemaitis et al. (2023) are shown as gray squares. We show the most probable double-Sérsic model from our MCMC analysis in orange, with the 68% range shown as the light orange envelope. Component 1 (representing F8D1’s remnant spheroid) is shown as a dashed dark blue curve, while Component 2 (representing the tidal stream) is shown as a dark green curve. In the topmost panel, we show the fractional residuals of each measurement relative to the error envelope from the best model. The data are very well fit, within the uncertainties, by the double-Sérsic model.

Stars formed in the burst 1–3 Gyrs ago represent a much higher fraction of the current stellar mass in F8D1’s outskirts ($\sim 39\%$), relative to its center ($\sim 11\%$). This indicates that F8D1 hosts an age gradient, rather than a purely phase-mixed population. Quenching appears to have occurred on similar timescales for the entire galaxy, including its tidal stream (§ 3.2). Updated fits to F8D1’s global structure indicate that it is a reasonably massive satellite, with $M_* \simeq 10^8 M_\odot$, and a large fraction of that mass is currently contained in its stream.

In this discussion, we reflect on F8D1’s evolutionary history and future as a tidally disrupting galaxy (§ 4.1), how it can help us understand the evolution of UDGs (§ 4.2), and how consideration of comparable progenitors illuminates the physical processes driving galaxy evolution at this mass scale (§ 4.3).

4.1. F8D1 as a Product of Tidal Disruption

The most obvious feature of F8D1 is its ongoing tidal disruption (Žemaitis et al. 2023). The HST-based measurements of F8D1’s SFH and global structure we

have presented in this paper place new constraints on F8D1’s orbital history and state of tidal disruption.

Both the deep central WFC3 field and the deep parallel ACS field show two significant recent bursts of star formation 2 Gyr and 500 Myr ago. Because our structural fits to F8D1 show that the ACS deep parallel field is dominated by F8D1’s stream, we can say that at least the inner part of F8D1’s tidal stream is < 500 Myr old, implying that its last pericenter from its main disturber was no more than 500 Myr ago. From our structural fits, the stellar mass of the central spheroidal component, which we take to signify the main body of F8D1, is $1.01^{+0.14}_{-0.13} \times 10^8 M_\odot$. Our shallow HST fields and the profiles from Žemaitis et al. (2023) cover only the Northern part of F8D1’s debris field; that Northern part of the stream contains $0.34^{+0.28}_{-0.20} \times 10^8 M_\odot$ in stars. In the case that the Northern stream is the only stream (i.e., if F8D1 is projected close to the stream apocenter), then the stream is 25% of the total system mass. If, instead, we assume that there is a symmetric tail to

Table 5. Global Properties of F8D1

Parameter	Value
$I_{e,1}$	$33.13^{+9.27}_{-5.79} \times 10^5 M_{\odot} \text{ kpc}^{-2}$
$R_{e,1}$	$1.86^{+0.12}_{-0.13} \text{ kpc}$
n_1	$0.43^{+0.16}_{-0.17}$
$M_{*,1}$	$9.93^{+1.63}_{-1.40} \times 10^7 M_{\odot}$
$I_{e,2}$	$1.02^{+0.19}_{-0.20} \times 10^5 M_{\odot} \text{ kpc}^{-2}$
$R_{e,2}$	$32.62^{+3.36}_{-2.11} \text{ kpc}$
n_2	$0.73^{+0.18}_{-0.14}$
$M_{*,2}^{\text{north}}$	$3.42^{+0.31}_{-0.21} \times 10^7 M_{\odot}$
$M_{*,\text{total}}$	$1.33^{+0.38}_{-0.14} \times 10^8 M_{\odot}$
Assuming $M/L_V = 1$	
$M_{V,\text{inner}}$	-15.2
$M_{V,\text{total}}$	-15.5
$\mu_{V,0}$	24.4
$\mu_{V,e}$	25.1
$\langle \mu_V \rangle_e$	24.7

NOTE—Derivation of fit parameters is described in §3.3. Components 1 and 2 are taken to be F8D1’s bound central spheroid and its tidal stream, respectively. Stellar masses include a typical lifetime mass loss of 40% for an evolved population.

the South that neither the Subaru nor HST data have imaged, the stream is 40% of the total system mass.

4.1.1. What is Responsible for F8D1’s Tidal Disruption?

Despite these new insights, the origin of F8D1’s tidal disruption remains uncertain. Its position in the M81 Group means that, without a bespoke modeling effort, its tidal features could equally likely result from interaction with M81, NGC 2976, or a combination of both. To investigate the tidal influence from each system, we first calculate the tidal index (see e.g., Karachentsev et al. 2014; Pearson et al. 2016), ignoring velocity and line-of-sight separation, and taking into account only the stellar mass of M81 and NGC 2976 respectively ($M_{*,M81} = 6.0 \times 10^{10} M_{\odot}$ and $M_{*,NGC\ 2976} = 1.9 \times 10^9 M_{\odot}$), and their projected separation from F8D1 ($R_{\text{proj},M81} = 120 \text{ kpc}$ and $R_{\text{proj},NGC\ 2976} = 33 \text{ kpc}$). We find that each system yields comparable and large tidal influence on F8D1, where $\Theta_{M81} = 2.54$ and $\Theta_{NGC\ 2976} = 2.72$. Note that the line-of-sight velocity separation between F8D1 and M81

is a factor of 3 smaller than between F8D1 and NGC 2976, -103 km s^{-1} (Forbes et al. 2024) vs. -34 km s^{-1} , but that the potential line-of-sight separation between F8D1 (which is assumed to be at $D_{\text{los}} = 3.8 \text{ Mpc}$ in this paper) and M81 (at $D_{\text{los}} = 3.6 \text{ Mpc}$; Radburn-Smith et al. 2011) is greater than the projected separation between F8D1 and NGC 2976. This distance difference is the primary uncertainty in establishing F8D1’s orbital history. Establishing distance moduli to galaxies in the M81 Group to better than $\sim 0.2 \text{ mag}$ is particularly difficult due to the substantially variable Galactic cirrus in this region. See Smercina et al. (2020) and Žemaitis et al. (2023) for deep, wide-field images of the M81 Group that show the variable cirrus throughout this region.

If the most recent bursts of star formation, around 500 Myr ago, was triggered by pericentric passages that helped produce the observed stream from F8D1, we can estimate the orbital velocity required for F8D1 to have passed near M81 or NGC 2976 at that time. To have passed close to M81 500 Myr ago, which is at least 120 kpc away (projected distance), F8D1 would need to move tangentially with a velocity of at least $\sim 235 \text{ km s}^{-1}$. To have passed close to NGC 2976 500 Myr ago, which is only 33 kpc away (projected distance), F8D1 would need to move tangentially with a velocity of at least $\sim 65 \text{ km s}^{-1}$. The line-of-sight velocity of F8D1 is $-103 \pm 36 \text{ km s}^{-1}$ (Forbes et al. 2024), while M81 and NGC 2976 have $v_r = -34 \text{ km s}^{-1}$ and $v_r = 3 \text{ km s}^{-1}$, respectively (de Vaucouleurs et al. 1991). Thus, the total velocity of F8D1 with respect to M81 and NGC 2976 would be $\sim -245 \text{ km s}^{-1}$ and $\sim -124 \text{ km s}^{-1}$, respectively.

In stellar mass, M81 is a MW analog and NGC 2976 is similar to the LMC. Assuming that their dark matter halo masses also follow estimates of the MW and LMC halo masses, this means that at distance of 120 kpc, F8D1 is likely bound to M81, and at a distance of 33 kpc F8D1 can also be bound to NGC 2976 — similar to the MW/LMC/SMC system. Here we ignore the line-of-sight distances as the errors on these are large. Thus, it seems likely that F8D1 could be bound to either host and that its stream could be produced from an interaction with either system.

To explore whether the earlier burst around 2 Gyr ago could correspond to a previous pericenter, it is helpful to compare to orbits of known systems. For example, the Sagittarius dwarf in the Milky Way shows how orbital phases can be connected to repeated star formation and stripping events. However, reaching a galactocentric radius of at least 120 kpc in 500 Myr, preceded by a pericenter pass 2 Gyr ago, might be difficult to ex-

plain for a Sagittarius-like dwarf galaxy system around a MW-like host (see orbital decays in Laporte et al. 2018; Hunt et al. 2021; Vasiliev et al. 2021, and Bell et al. in prep.). If an interaction with NGC 2976 is responsible for the formation of F8D1’s tidal stream and its two most recent bursts in star formation, the scenario resembles a dwarf-dwarf interaction, similar to the LMC–SMC or NGC 4490–4485 systems (Besla et al. 2012; Pearson et al. 2018). The orbits of these dwarf-pair analogs and orbits of dwarf pairs analyzed from TNG100 in Chamberlain et al. (2024) show that a pericenter of a few $\times 100$ Myr, preceded by a pericenter ~ 2 Gyr ago, is plausible. It is also possible that the stream is formed due to a combination of ‘pre-processing’ due to gravitational interaction with NGC 2976 and tidal forces from M81. Future detailed modeling is necessary to determine which explanation is more likely, and to better constrain the nature of the interaction.

4.1.2. Comparison With Other Nearby Disrupting Satellites

Here we compare F8D1’s current state of disruption against other known examples of disrupting satellites. Two galaxies in nearby groups are at somewhat earlier stages in their disruption, but already show important effects from tides on their main bodies. NGC 147 is a satellite in the M31 group with $M_\star \sim 6 \times 10^8 M_\odot$ (Geha et al. 2010) with tidal arms that may contain $\sim 10\%$ of its total mass (Arias et al. 2016). NGC 147’s main body exhibits isophote twists, showing that its main body is significantly affected by tides (Crnojević et al. 2014). NGC 3077, a roughly LMC-mass member of the M81 group, is at a similar stage in its disruption as NGC 147, with $\sim 13\%$ of its stellar mass in its tidal envelope (Smercina et al. 2020) and a similar *S*-shaped morphology (e.g., Okamoto et al. 2023). In NGC 3077’s case, almost all of its H I gas has already been stripped from it in its interaction with M81 (Walter et al. 2002; de Blok et al. 2018), and the remaining gas is being rapidly consumed in a modest starburst with $t_{\text{dep}} \sim 10$ Myr (Meier et al. 2001).

In contrast, the Sagittarius dwarf spheroidal (Sgr) and its stream appear to be a similar system to F8D1, just at a much later stage in its disruption. We note that while Sgr is the closest example, it several satellites in nearby galaxy groups have been identified that closely resemble Sagittarius in their bulk properties and state of disruption, such as Scl-MM-Dw2 around NGC 253 (Toloba et al. 2016), and CenA-MM-Dw3 around Centaurus A (Crnojević et al. 2016). While the total mass, half-light radius, and metallicity of Sgr are all very similar to F8D1 (see McConnachie 2012 and Figure 2), there are some important differences. First, Sgr is more

disrupted (70% of the mass is in the tails; Niederste-Ostholt et al. 2010 vs. 25–40% in the tails for F8D1). The SFH of Sgr’s tidal tails and core (Siegel et al. 2007) show a major drop in SFR ~ 3 –5 Gyr ago (Siegel et al. 2007; Weisz et al. 2014; de Boer et al. 2015), although Sgr’s core experienced a significant episode of more recent star formation ~ 2.5 –3 Gyr ago, with some possibly younger stars (Siegel et al. 2007; Weisz et al. 2014). The metallicity of the most recently-formed stars appear quite similar to F8D1 ($[M/H] \sim -0.5$; compare Figure 9 with e.g., Hasselquist et al. 2021). Because Sgr is so close to the MW, its chemical evolution is more richly constrained, showing α/Fe trends lower than the Milky Way for most metallicities (consistent with its lower total mass and star formation efficiency), showing a flattening in α/Fe for the most recent star formation as α element production kept pace with Iron production from Type Ia Supernovae (Hasselquist et al. 2021). The overall picture is that F8D1 is quite consistent with a less evolved version of Sgr.

4.2. How Does F8D1 Inform Our Ideas About UDG Formation?

UDGs are a heterogeneous group of galaxies, brought together by virtue of very low central surface brightness ($\mu_{0,V} \gtrsim 23$ –24 mag arcsec $^{-2}$) and extended half-light radii ($R_{\text{eff}} = 2$ –4 kpc; e.g., van Dokkum et al. 2015a, Zaritsky et al. 2023). While originally explored in the Coma galaxy cluster (van Dokkum et al. 2015a), UDGs have been discovered in a wide range of environments. UDGs occur as satellites in groups all the way from the Milky Way’s group mass scale to large galaxy clusters (e.g., van der Burg et al. 2017; Lim et al. 2020; Karunakaran & Zaritsky 2023; Zaritsky et al. 2023). Most of these satellite UDGs in clusters and groups lack ongoing star formation, while those in isolated environments can have very high gas content, relative to their stars, and host current star formation (e.g., Papastergis et al. 2017; He et al. 2019; Prole et al. 2019; Kadowaki et al. 2021). Some UDGs have exceptionally high inferred mass-to-light (M/L) ratios, indicating a high degree of dark matter domination (see e.g., Kravtsov 2024), while others have M/L values in the range consistent with stellar populations alone (e.g., van Dokkum et al. 2018; Toloba et al. 2018; van Dokkum et al. 2019; Toloba et al. 2023). It is virtually certain that there are a number of mechanisms that lead to UDGs, with various mechanisms being more or less important depending on the particular types of UDG being studied. Indeed, many theoretical studies find that multiple mechanisms — internal to the galaxy and external to the galaxy — should operate in concert to give a realistic range of

UDGs. Accordingly, we do not attempt to ‘solve’ the issue of UDG formation using F8D1. Instead, here we reflect on how F8D1, as a case study, illuminates certain UDG formation scenarios.

4.2.1. *Star Formation Histories of UDGs*

Many of the formation mechanisms for UDGs are connected to important signatures in their SFHs. F8D1’s early star formation history is relatively uncertain, with $\sim 80\%$ of its stars forming before ~ 6 Gyr ago. There was a prominent episode of star formation 2–2.5 Gyr ago in which $\sim 15\text{--}20\%$ of its stars formed ($\sim 15\%$ in the central field, $\sim 45\%$ in the deep ACS inner stream field). An additional episode of star formation happened ~ 500 Myr ago, in which a few percent of its stars formed. In this section, we will briefly discuss how F8D1’s SFH compares with the signatures of possible UDG formation models. This discussion is necessarily tentative, in great part because F8D1’s UDG nature may be dominated by the impacts of tides (and other environmental processes).

Several papers emphasize that intense feedback from bursty star formation, which is pivotal in DM core creation, has the consequence of lowering the central density of $M_\star \sim 10^8 M_\odot$ galaxies, and can lead to the formation of UDGs (e.g., [El-Badry et al. 2016](#); [Di Cintio et al. 2017](#); [Chan et al. 2018](#)). F8D1 shows some features consistent with this picture. Where the SFH is well-resolved, F8D1 clearly shows multiple bursts of SF at ~ 2 Gyr and ~ 500 Myr ago. Yet, there are some areas where the F8D1’s properties appear to differ from the theoretical expectations. F8D1’s SFH before ~ 2 Gyr ago is concentrated at early times (with substantial SFH uncertainties), but not outwardly similar to the kind of ~ 300 Myr–2 Gyr starburst cadence characteristic of the simulations from [El-Badry et al. \(2016\)](#) or [Di Cintio et al. \(2017\)](#). In addition, the models suggest that the oldest stars should have experienced the most radial migration, resulting in preferentially older outer parts. This is in contrast to F8D1’s age gradient, which shows outskirts that are clearly younger than the center (τ_{80} of < 2 Gyr vs. > 6 Gyr, respectively; see [Figure 6](#) and [Table 3](#)). Obviously, the interpretation of the observations is complicated by F8D1’s extensive tidal processing, and a DM core sculpted by bursty star formation would strongly change the impact of tides on F8D1. We conclude that F8D1’s SFH shows some consistency with a bursty SF picture, but with some differences (e.g., early star formation and younger outskirts) that are not trivially interpreted in such a picture.

The SFH implications of UDGs as the high angular momentum tail of the dwarf galaxy population

(e.g., [Dalcanton et al. 1997](#); [Amorisco & Loeb 2016](#); [Liao et al. 2019](#)) are somewhat unclear. The naive expectation of such a picture might be that star formation should proceed more or less continuously with low efficiency (e.g., [Benavides et al. 2024](#)), in diffuse H I disks over long timescales, similar to their star-forming low surface brightness galaxy siblings ([de Blok et al. 1996](#); [Bell et al. 2000](#); [Schombert & McGaugh 2014](#)). In contrast, F8D1 experienced much of its SF at relatively early times, but did retain the gas necessary to make $\gtrsim 20\%$ of its stellar mass in late star formation $\lesssim 4$ Gyr ago. F8D1’s more recent star formation was likely entirely driven by tidal interaction, however, and does not necessarily invalidate a ‘high-spin’ formation scenario.

F8D1’s properties do not strongly align with the expectations of a ‘failed galaxy’ picture of UDG formation. In this picture, these ‘failed’ UDGs stop forming stars early, $z \sim 2$, leaving a remnant with an unusually high number of globular clusters for their stellar mass and no current SF ([van Dokkum et al. 2015a](#); [Peng & Lim 2016](#); [Ferré-Mateu et al. 2018](#)). In this picture, environmental processes (e.g., ram pressure) are usually credited with causing the early cessation of star formation. Visual inspection of our HST images shows 6 globular cluster candidates, including the GC already discovered by [Caldwell et al. \(1998\)](#). This number is similar to the number of globular clusters in galaxies of a similar mass (e.g., Fornax, [Pace et al. 2021](#); Sagittarius dwarf spheroidal and stream, [Bellazzini et al. 2020](#); and many of the UDGs found in clusters, e.g., [Lim et al. 2020](#); [Toloba et al. 2023](#)), indicating no dramatic deficit of stellar mass compared to its globular cluster number or inferred dark matter mass. On the balance, F8D1’s late-time star formation and reasonably typical globular cluster number argue against a ‘failed galaxy’ origin for F8D1.

One can see that F8D1 shows aspects of many of the factors that are thought to shape UDG formation and evolution. It had an initial episode of star formation that was followed by a fallow period, consistent broadly with a bursty formation scenario (or a failed ‘failure’!). Yet, F8D1 retained a reservoir of gas (consistent with bursty or high angular momentum scenario) that fueled further bursts of star formation ~ 2 Gyr and ~ 500 Myr ago. Importantly, the dominant driver of F8D1’s recent evolution is tidal processing, which may have contributed to (or triggered) F8D1’s most recent SF bursts, and created tidal tails containing 25–40% of its total stellar mass.

4.2.2. The Importance of Tides in UDG Formation

One point that is exceptionally clear, from both this work and Žemaitis et al. (2023), is the importance of tides in shaping F8D1, and by extension, in shaping at least some UDGs. Isolated UDGs are, obviously, not expected to have been affected by tides. Deep imaging studies in groups do not find tidal tails around some UDGs (e.g., NGC 1052’s UDGs; Müller et al. 2019, although see also Montes et al. 2020 who claim tidal debris around NGC1052-DF4), but find the impacts of environmental processing in the forms of ram pressure stripping and/or tidal tails around other group UDGs (e.g., Bennet et al. 2018; Gannon et al. 2021; Fielder et al. 2024; Watts et al. 2024), and even more exotic dwarf merger scenarios (e.g., van Dokkum et al. 2022; Keim et al. 2025).

An important factor in determining the response of a satellite galaxy to tides is the structure of the central parts of its dark matter halo. Galaxies with cusped DM halo profiles do not substantially change in their central structure during a tidal interaction, while galaxies with cored dark matter halos ‘puff up’ substantially as they are tidally stripped (e.g., Errani et al. 2015; Carleton et al. 2019). Velocity profiles indicative of cores are particularly common in galaxies with stellar masses $\sim 10^8 M_\odot$ (both non-star-forming spheroidal galaxies and star-forming irregulars; e.g., Battaglia et al. 2008; Walker & Peñarrubia 2011; Oh et al. 2011). Galaxies simulated in a Λ CDM cosmological framework require strong effects from stellar feedback to produce such strongly cored dark matter density profiles, which on one hand requires enough star formation to inject a large enough amount of energy, and on the other hand a shallow enough potential to allow the outflows to significantly affect the distribution of the ISM (e.g., Pontzen & Governato 2012; Di Cintio et al. 2014; Chan et al. 2015; Lazar et al. 2020). This favors core formation in a broad stellar mass range centered on $M_\star \sim 10^{8.5} M_\odot$, similar in mass to F8D1.

We can estimate the magnitude of this increase in size for a cored progenitor of F8D1, using the framework of Errani et al. (2015). As discussed in § 4.1.2, F8D1’s tidal streams contain 25–40% of its stellar mass. Errani et al. (2015) suggest that this degree of stellar mass loss indicates a loss of 80–90% of its total mass. For this degree of mass loss, negligible changes in R_e would be expected for a cusped DM density profile. In contrast, for a cored profile, Errani et al. (2015) predicts a factor of 2.5–4 increase in R_e . This suggests that F8D1’s progenitor may have had a significant core and been substantially more compact than its current half-light radius (~ 1.9 kpc), with half-light radii between 500 pc

and 1 kpc. We will use this information in § 4.3 where we consider possible progenitor analogs for F8D1.

4.3. Reflections on Possible F8D1 Progenitors

In the light of these different formation scenarios, it is interesting to reflect on possible progenitors of the F8D1 system. If F8D1 experienced no increase in its half-light radius (~ 1.9 kpc in its main body; this work) owing to tides, then there are a limited number of analogs of ‘star-forming F8D1s’. The largest samples of analogs are drawn from larger volume catalogs. For example, Janowiecki et al. (2019) identify a sample of 71 H I-rich UDGs with $M_g \sim -16$ and $R_e > 1.5$ kpc, with H I masses around $\sim 10^9 M_\odot$, that might represent star-forming progenitors of F8D1 (see also Leisman et al. 2017). Although the identification of 71 progenitors seems like such galaxies might be common, these galaxies were selected from a parent sample of more than 15,000 H I-bearing galaxies between $25 < D/\text{Mpc} < 120$; star-forming UDGs are reasonably rare. In addition, consideration of their star formation rates and histories suggests that they remain ultra-diffuse by virtue of a low star formation efficiency over much of the lifetime of the Universe (Kado-Fong et al. 2022), perhaps somewhat at variance with F8D1’s SFH, in which $\sim 80\%$ of its stars were formed > 6 Gyr ago or more.

If F8D1’s half-light radius has increased as part of the process of tidal stripping, owing to a cored mass profile (e.g., Errani et al. 2015), then possible progenitor (and descendant) systems can be identified more readily, to the point where an ‘evolutionary sequence’ can be envisaged using galaxies in the Local Group alone. Among Local Group members, NGC 6822 and IC 1613 are the closest star-forming galaxies in stellar masses to F8D1, with H I masses of $1.3 \times 10^8 M_\odot$ (de Blok & Walter 2000) and $5 \times 10^7 M_\odot$ (Silich et al. 2006), respectively. IC 1613’s may be experiencing initial tidal disruption/processing, as evidenced both in its distribution of stars and H I (Battinelli et al. 2007), and, as discussed in § 4.1.2, Sagittarius is a plausible descendant system. We illustrate the comparison between F8D1 and its local analogs schematically in Figure 14. We compare the surface brightnesses, sizes, visual appearances and SFHs of NGC 6822, IC 1613, F8D1 and Sagittarius. The galaxies exhibit monotonic trends in all four properties with stage of tidal disruption. We therefore postulate that increasing impacts of tidal processing puffs up the stellar distribution, decreases the central density, and is reflected on the SFH by later τ_{90} values, as star formation is quenched by the effects of group ram pressure. In this paradigm, F8D1 represents an intermediate stage of a

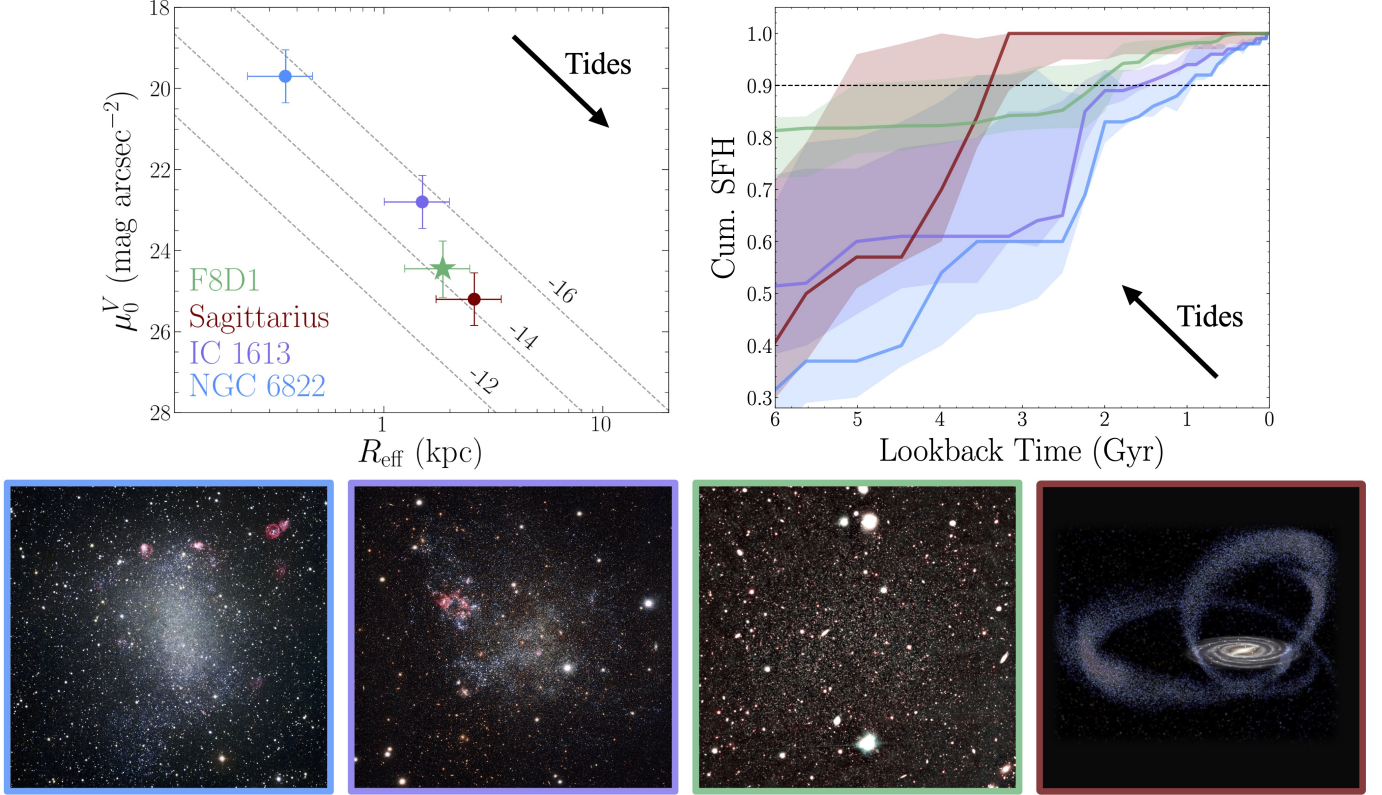


Figure 14. Comparison of F8D1’s (green) properties measured in this work to those of local galaxies with analogous progenitor stellar mass: NGC 6822 (blue), IC 1613 (purple), and Sagittarius (dark red). *Top Left:* Effective radius vs. central V-band surface brightness for F8D1 and the three Local Group galaxies. As in Figure 2, lines of constant M_V have been drawn, assuming exponential profiles. Note that none of the four galaxies’ light profiles follow a true exponential, and therefore these are guides. We assume a consistent 33% on the effective radii. *Top Right:* Combined cumulative SFHs of the four galaxies over the past 6 Gyr (this work and Weisz et al. 2014). Note that Sagittarius combines fields along the stream and the remnant dwarf spheroidal. In both spaces, the four galaxies form a plausible evolutionary sequence, where tidal processing similarly impacts both the morphology and star formation in dwarf galaxies at this mass scale. NGC 6822 and IC 1613 are currently star-forming and are plausible analogs of F8D1’s progenitor, while Sagittarius is in a more advanced stage of tidal disruption.

Images: From left to right — $B/V/R/H\alpha$ image of NGC 6822 from the 2.2m MPG/ESO telescope at La Silla Observatory; $U/G/R/H\alpha$ image of IC 1613 from OmegaCAM on ESO’s VLT Survey Telescope; r/i color image of F8D1 from Subaru HSC; artistic representation of the interaction between Sagittarius and the Milky Way, from Gabriel Pérez Díaz at the Instituto de Astrofísica de Canarias (IAC).

common evolutionary pathway experienced by satellite galaxies at this mass scale.

It is worth briefly considering the fate of F8D1’s ISM in this scenario. Attributing specific features of the complex H I field in the M81 Group to specific galaxies will require a detailed orbital modeling effort (see §4.1.1). However, we note that the Eastern ‘arm’ of H I visible in the map of de Blok et al. (2018) (see Figure 1), which visually overlaps the end of F8D1’s stellar stream, contains $\sim 10^8 M_\odot$ of gas — highly comparable to the current reservoir of NGC 6822, and possibly to the expected pre-infall reservoir of F8D1. It is viable that this arm originally resided in the larger NGC 2976, which may also be experiencing ram pressure effects (e.g., Drzazga et al. 2016). However, NGC 2976 is still star-forming and does not appear to show a substan-

tial environmental impact (either positive or negative) in its recent SFH. Part of our future modeling effort will be to investigate whether this H I feature could comprise the ram pressure-stripped remnants of F8D1’s former ISM.

5. CONCLUSIONS

We have used new HST observations to infer the star formation history of the nearby UDG, F8D1, over the past 6 Gyr, using detections of individual stars to below the Red Clump in a central WFC3 field and an outer ACS field. Using detected evolved RGB and AGB stars in a set of shallower WFC3+ACS fields, in concert with published Subaru HSC observations, we have measured the properties of F8D1’s main body and stellar stream. This temporal and morphological study of

F8D1 represents one of the most detailed case studies of a UDG to-date. We find:

1. Three distinct periods of star formation; the first, >6 Gyr ago, when $\sim 80\%$ of F8D1's stars formed (with considerable uncertainties). This was followed by a burst of star formation $\sim 2\text{--}2.5$ Gyr ago, that formed $\sim 11\%$ of the stars in the central field and $\sim 39\%$ in the outer field. Lastly, a smaller burst occurred only ~ 500 Myr ago, forming a few % of F8D1's stars, and which also likely formed F8D1's nuclear star cluster.
2. A global shutdown time of <2 Gyr in F8D1, including its core and tidal stream out to 13 kpc, combining the SFH fits with the ratio of AGB-to-upper RGB stars. This indicates that F8D1 was globally star-forming 2 Gyr ago.
3. A two-component morphology, with a total progenitor stellar mass of $1.33^{+0.38}_{-0.14} \times 10^8 M_{\odot}$. An MCMC fitting analysis yields two distinct Sérsic components to its stellar mass surface density profile: an inner spheroid, with a half-light radius of 1.9 kpc, and an extended tidal stream, with a half-light radius of 33 kpc. Our new structural model of F8D1 predicts that 25–40% of its stellar mass is currently unbound in this extensive tidal stream.
4. The outer deep field, which lies on the inner portion of F8D1's stream, was star-forming 500 Myr ago, constraining the formation time of the inner portion of the stream.
5. It is as yet unclear whether M81 or NGC 2976 are responsible for environmentally processing F8D1; both are plausible interaction partners when taking into account projected separations, line-of-sight distances, and velocities. One or both of F8D1's recent bursts of star formation may be associated with pericenter passages, but the recent star formation in F8D1's tidal tail constrains its most recent pericenter to <500 Myr ago. More detailed orbital modeling, deeper mapping of F8D1's tidal streams, and/or more careful consideration of distance constraints and F8D1's SFH, will be necessary to clarify F8D1's tidal history.
6. F8D1's bursty star formation history illustrates characteristics anticipated by theoretical models that link such histories with the 'puffing up' of a galaxy through strong episodic stellar feedback, leading to DM core formation. The presence of significant star formation late in its history, however, alongside its seemingly typical globular cluster population, argues against a 'failed galaxy' scenario for F8D1's origin.

While a variety of UDG formation pathways are necessary to account for the full diversity of these low surface brightness galaxies, F8D1 underlines and richly illustrates the importance of environment, and tidal processing particularly, in forming UDGs. Simulations of the tidal disruption of satellites residing in cored potentials, as expected at F8D1's stellar mass scale, predict substantial morphological changes and size increases for tidally-disrupting satellites at F8D1's stage of disruption. In this paradigm, we find that plausible progenitors for F8D1 exist in the local universe, irrespective of how strongly tidal processing affects the central surface brightness of satellites. In the (likely) event that F8D1 has a cored density profile, F8D1's progenitor may have had properties similar to Local Group galaxies NGC 6822 and IC 1613, illustrating a possible sequence from star-forming dwarf irregular, to an ultra-diffuse galaxy undergoing tidal disruption (F8D1), eventually resulting in a more mature stream system like the Sagittarius dwarf spheroidal and its stream at later times.

Facility: Hubble Space Telescope (ACS, WFC3), MAST, Subaru Telescope (HSC)

Software: MATCH (Dolphin 2002), DOLPHOT (Dolphin 2016), Matplotlib (Hunter 2007), NumPy (Oliphant 2006; Van Der Walt et al. 2011), Astropy (Astropy Collaboration et al. 2018), SciPy (Virtanen et al. 2020), SAOImage DS9 (Smithsonian Astrophysical Observatory 2000)

ACKNOWLEDGMENTS

This research is based on observations made with the NASA/ESA Hubble Space Telescope, associated with program GO-16191, and obtained from the Space Telescope Science Institute. AS is supported by NASA through the NASA Hubble Fellowship grant HST-HF2-51567, also awarded by the Space Telescope Science Institute. The Space Telescope Science Institute is operated by the Association of Universities for Research in Astronomy, Inc., under NASA contract NAS 5-26555. ET is thankful for the support from NSF-AST- 2206498 grant. AM acknowledges support from the ANID FONDECYT Regular grant 1251882, from the ANID BASAL project FB210003, and funding from the HORIZON-MSCA-2021-SE-01 Research and Innovation Programme under the Marie Skłodowska-Curie grant agreement number 101086388.

REFERENCES

- Albers, S. M., Weisz, D. R., Cole, A. A., et al. 2019, *MNRAS*, 490, 5538, doi: [10.1093/mnras/stz2903](https://doi.org/10.1093/mnras/stz2903)
- Alves, D. R., & Sarajedini, A. 1999, *ApJ*, 511, 225, doi: [10.1086/306655](https://doi.org/10.1086/306655)
- Amorisco, N. C., & Loeb, A. 2016, *MNRAS*, 459, L51, doi: [10.1093/mnras/slw055](https://doi.org/10.1093/mnras/slw055)
- Amorisco, N. C., Monachesi, A., Agnello, A., & White, S. D. M. 2018, *MNRAS*, 475, 4235, doi: [10.1093/mnras/sty116](https://doi.org/10.1093/mnras/sty116)
- Arias, V., Guglielmo, M., Fernando, N., et al. 2016, *MNRAS*, 456, 1654, doi: [10.1093/mnras/stv2781](https://doi.org/10.1093/mnras/stv2781)
- Astropy Collaboration, Price-Whelan, A. M., Sipőcz, B. M., et al. 2018, *AJ*, 156, 123, doi: [10.3847/1538-3881/aabc4f](https://doi.org/10.3847/1538-3881/aabc4f)
- Barbosa, C. E., Zaritsky, D., Donnerstein, R., et al. 2020, arXiv e-prints, arXiv:2002.05171. <https://arxiv.org/abs/2002.05171>
- Battaglia, G., Helmi, A., Tolstoy, E., et al. 2008, *ApJL*, 681, L13, doi: [10.1086/590179](https://doi.org/10.1086/590179)
- Battinelli, P., Demers, S., & Artigau, É. 2007, *A&A*, 466, 875, doi: [10.1051/0004-6361:20066578](https://doi.org/10.1051/0004-6361:20066578)
- Bell, E. F., Barnaby, D., Bower, R. G., et al. 2000, *MNRAS*, 312, 470, doi: [10.1046/j.1365-8711.2000.03180.x](https://doi.org/10.1046/j.1365-8711.2000.03180.x)
- Bellazzini, M., Ibata, R., Malhan, K., et al. 2020, *A&A*, 636, A107, doi: [10.1051/0004-6361/202037621](https://doi.org/10.1051/0004-6361/202037621)
- Benavides, J. A., Sales, L. V., Abadi, M. G., et al. 2024, *ApJ*, 977, 169, doi: [10.3847/1538-4357/ad8de8](https://doi.org/10.3847/1538-4357/ad8de8)
- Bennet, P., Sand, D. J., Zaritsky, D., et al. 2018, *ApJL*, 866, L11, doi: [10.3847/2041-8213/aadedf](https://doi.org/10.3847/2041-8213/aadedf)
- Besla, G., Kallivayalil, N., Hernquist, L., et al. 2012, *MNRAS*, 421, 2109, doi: [10.1111/j.1365-2966.2012.20466.x](https://doi.org/10.1111/j.1365-2966.2012.20466.x)
- Blakeslee, J. P., Jordán, A., Mei, S., et al. 2009, *ApJ*, 694, 556, doi: [10.1088/0004-637X/694/1/556](https://doi.org/10.1088/0004-637X/694/1/556)
- Bressan, A., Marigo, P., Girardi, L., et al. 2012, *MNRAS*, 427, 127, doi: [10.1111/j.1365-2966.2012.21948.x](https://doi.org/10.1111/j.1365-2966.2012.21948.x)
- Burkert, A. 2017, *ApJ*, 838, 93, doi: [10.3847/1538-4357/aa671c](https://doi.org/10.3847/1538-4357/aa671c)
- Caldwell, N., Armandroff, T. E., Da Costa, G. S., & Seitzer, P. 1998, *AJ*, 115, 535, doi: [10.1086/300233](https://doi.org/10.1086/300233)
- Carleton, T., Errani, R., Cooper, M., et al. 2019, *MNRAS*, 485, 382, doi: [10.1093/mnras/stz383](https://doi.org/10.1093/mnras/stz383)
- Chamberlain, K., Patel, E., Besla, G., Torrey, P., & Rodriguez-Gomez, V. 2024, *ApJ*, 975, 104, doi: [10.3847/1538-4357/ad7bad](https://doi.org/10.3847/1538-4357/ad7bad)
- Chan, T. K., Kereš, D., Oñorbe, J., et al. 2015, *MNRAS*, 454, 2981, doi: [10.1093/mnras/stv2165](https://doi.org/10.1093/mnras/stv2165)
- Chan, T. K., Kereš, D., Wetzel, A., et al. 2018, *MNRAS*, 478, 906, doi: [10.1093/mnras/sty1153](https://doi.org/10.1093/mnras/sty1153)
- Cioni, M. R. L., Girardi, L., Marigo, P., & Habing, H. J. 2006, *A&A*, 448, 77, doi: [10.1051/0004-6361:20053933](https://doi.org/10.1051/0004-6361:20053933)
- Collins, M. L. M., Williams, B. F., Tollerud, E. J., et al. 2022, *MNRAS*, 517, 4382, doi: [10.1093/mnras/stac2794](https://doi.org/10.1093/mnras/stac2794)
- Crnojević, D., Ferguson, A. M. N., Irwin, M. J., et al. 2014, *MNRAS*, 445, 3862, doi: [10.1093/mnras/stu2003](https://doi.org/10.1093/mnras/stu2003)
- Crnojević, D., Sand, D. J., Spekkens, K., et al. 2016, *ApJ*, 823, 19, doi: [10.3847/0004-637X/823/1/19](https://doi.org/10.3847/0004-637X/823/1/19)
- Dalcanton, J. J., Spergel, D. N., Gunn, J. E., Schmidt, M., & Schneider, D. P. 1997, *AJ*, 114, 635, doi: [10.1086/118499](https://doi.org/10.1086/118499)
- Danieli, S., van Dokkum, P., Conroy, C., Abraham, R., & Romanowsky, A. J. 2019, *ApJL*, 874, L12, doi: [10.3847/2041-8213/ab0e8c](https://doi.org/10.3847/2041-8213/ab0e8c)
- de Blok, W. J. G., & McGaugh, S. S. 1997, *MNRAS*, 290, 533, doi: [10.1093/mnras/290.3.533](https://doi.org/10.1093/mnras/290.3.533)
- de Blok, W. J. G., McGaugh, S. S., & van der Hulst, J. M. 1996, *MNRAS*, 283, 18, doi: [10.1093/mnras/283.1.18](https://doi.org/10.1093/mnras/283.1.18)
- de Blok, W. J. G., & Walter, F. 2000, *ApJL*, 537, L95, doi: [10.1086/312777](https://doi.org/10.1086/312777)
- de Blok, W. J. G., Walter, F., Ferguson, A. M. N., et al. 2018, *ApJ*, 865, 26, doi: [10.3847/1538-4357/aad557](https://doi.org/10.3847/1538-4357/aad557)
- de Boer, T. J. L., Belokurov, V., & Koposov, S. 2015, *MNRAS*, 451, 3489, doi: [10.1093/mnras/stv946](https://doi.org/10.1093/mnras/stv946)
- de Vaucouleurs, G., de Vaucouleurs, A., Corwin, Jr., H. G., et al. 1991, Third Reference Catalogue of Bright Galaxies
- Di Cintio, A., Brook, C. B., Dutton, A. A., et al. 2017, *MNRAS*, 466, L1, doi: [10.1093/mnras/slw210](https://doi.org/10.1093/mnras/slw210)
- Di Cintio, A., Brook, C. B., Macciò, A. V., et al. 2014, *MNRAS*, 437, 415, doi: [10.1093/mnras/stt1891](https://doi.org/10.1093/mnras/stt1891)
- Dolphin, A. 2016, DOLPHOT: Stellar photometry, Astrophysics Source Code Library, record ascl:1608.013
- Dolphin, A. E. 2000, *PASP*, 112, 1383, doi: [10.1086/316630](https://doi.org/10.1086/316630)
- . 2002, *MNRAS*, 332, 91, doi: [10.1046/j.1365-8711.2002.05271.x](https://doi.org/10.1046/j.1365-8711.2002.05271.x)
- . 2012, *ApJ*, 751, 60, doi: [10.1088/0004-637X/751/1/60](https://doi.org/10.1088/0004-637X/751/1/60)
- . 2013, *ApJ*, 775, 76, doi: [10.1088/0004-637X/775/1/76](https://doi.org/10.1088/0004-637X/775/1/76)
- Drzazga, R. T., Chyży, K. T., Heald, G. H., Elstner, D., & Gallagher, J. S. 2016, *A&A*, 589, A12, doi: [10.1051/0004-6361/201527236](https://doi.org/10.1051/0004-6361/201527236)
- Duane, S., Kennedy, A. D., Pendleton, B. J., & Roweth, D. 1987, *Physics Letters B*, 195, 216, doi: [10.1016/0370-2693\(87\)91197-X](https://doi.org/10.1016/0370-2693(87)91197-X)
- El-Badry, K., Wetzel, A., Geha, M., et al. 2016, *ApJ*, 820, 131, doi: [10.3847/0004-637X/820/2/131](https://doi.org/10.3847/0004-637X/820/2/131)
- Errani, R., Penarrubia, J., & Tormen, G. 2015, *MNRAS*, 449, L46, doi: [10.1093/mnras/slv012](https://doi.org/10.1093/mnras/slv012)
- Ferré-Mateu, A., Gannon, J. S., Forbes, D. A., et al. 2023, *MNRAS*, 526, 4735, doi: [10.1093/mnras/stad3102](https://doi.org/10.1093/mnras/stad3102)

- Ferré-Mateu, A., Alabi, A., Forbes, D. A., et al. 2018, *MNRAS*, 479, 4891, doi: [10.1093/mnras/sty1597](https://doi.org/10.1093/mnras/sty1597)
- Fielder, C., Jones, M. G., Sand, D. J., et al. 2024, *AJ*, 168, 212, doi: [10.3847/1538-3881/ad74f6](https://doi.org/10.3847/1538-3881/ad74f6)
- Forbes, D. A., Lyon, D., Gannon, J., Romanowsky, A. J., & Brodie, J. P. 2024, *PASA*, 41, e044, doi: [10.1017/pasa.2024.41](https://doi.org/10.1017/pasa.2024.41)
- Gallart, C., Monelli, M., Ruiz-Lara, T., et al. 2021, *ApJ*, 909, 192, doi: [10.3847/1538-4357/abddbe](https://doi.org/10.3847/1538-4357/abddbe)
- Gannon, J. S., Dullo, B. T., Forbes, D. A., et al. 2021, *MNRAS*, 502, 3144, doi: [10.1093/mnras/stab277](https://doi.org/10.1093/mnras/stab277)
- Geha, M., van der Marel, R. P., Guhathakurta, P., et al. 2010, *ApJ*, 711, 361, doi: [10.1088/0004-637X/711/1/361](https://doi.org/10.1088/0004-637X/711/1/361)
- Girardi, L. 2016, *ARA&A*, 54, 95, doi: [10.1146/annurev-astro-081915-023354](https://doi.org/10.1146/annurev-astro-081915-023354)
- Girardi, L., Bressan, A., Bertelli, G., & Chiosi, C. 2000, *A&AS*, 141, 371, doi: [10.1051/aas:2000126](https://doi.org/10.1051/aas:2000126)
- Girardi, L., Williams, B. F., Gilbert, K. M., et al. 2010, *ApJ*, 724, 1030, doi: [10.1088/0004-637X/724/2/1030](https://doi.org/10.1088/0004-637X/724/2/1030)
- Gordon, K. D., Fouesneau, M., Arab, H., et al. 2016, *ApJ*, 826, 104, doi: [10.3847/0004-637X/826/2/104](https://doi.org/10.3847/0004-637X/826/2/104)
- Harmsen, B., Bell, E. F., D’Souza, R., et al. 2023, *MNRAS*, 525, 4497, doi: [10.1093/mnras/stad2480](https://doi.org/10.1093/mnras/stad2480)
- Hasselquist, S., Hayes, C. R., Lian, J., et al. 2021, *ApJ*, 923, 172, doi: [10.3847/1538-4357/ac25f9](https://doi.org/10.3847/1538-4357/ac25f9)
- He, M., Wu, H., Du, W., et al. 2019, *ApJ*, 880, 30, doi: [10.3847/1538-4357/ab2710](https://doi.org/10.3847/1538-4357/ab2710)
- Hogg, D. W., Bovy, J., & Lang, D. 2010, arXiv e-prints, arXiv:1008.4686, doi: [10.48550/arXiv.1008.4686](https://doi.org/10.48550/arXiv.1008.4686)
- Hunt, J. A. S., Stelea, I. A., Johnston, K. V., et al. 2021, *MNRAS*, 508, 1459, doi: [10.1093/mnras/stab2580](https://doi.org/10.1093/mnras/stab2580)
- Hunter, J. D. 2007, *Computing in Science and Engineering*, 9, 90, doi: [10.1109/MCSE.2007.55](https://doi.org/10.1109/MCSE.2007.55)
- Ibata, R. A., Gilmore, G., & Irwin, M. J. 1995, *MNRAS*, 277, 781, doi: [10.1093/mnras/277.3.781](https://doi.org/10.1093/mnras/277.3.781)
- Janowiecki, S., Jones, M. G., Leisman, L., & Webb, A. 2019, *MNRAS*, 490, 566, doi: [10.1093/mnras/stz1868](https://doi.org/10.1093/mnras/stz1868)
- Jones, M. G., Karunakaran, A., Bennet, P., et al. 2023, *ApJL*, 942, L5, doi: [10.3847/2041-8213/acaab](https://doi.org/10.3847/2041-8213/acaab)
- Kado-Fong, E., Greene, J. E., Huang, S., & Goulding, A. 2022, *ApJ*, 941, 11, doi: [10.3847/1538-4357/ac9964](https://doi.org/10.3847/1538-4357/ac9964)
- Kadowaki, J., Zaritsky, D., Donnerstein, R. L., et al. 2021, *ApJ*, 923, 257, doi: [10.3847/1538-4357/ac2948](https://doi.org/10.3847/1538-4357/ac2948)
- Karachentsev, I. D., Kaisina, E. I., & Makarov, D. I. 2014, *AJ*, 147, 13, doi: [10.1088/0004-6256/147/1/13](https://doi.org/10.1088/0004-6256/147/1/13)
- Karunakaran, A., & Zaritsky, D. 2023, *MNRAS*, 519, 884, doi: [10.1093/mnras/stac3622](https://doi.org/10.1093/mnras/stac3622)
- Keim, M. A., van Dokkum, P., Shen, Z., et al. 2025, arXiv e-prints, arXiv:2506.10220, doi: [10.48550/arXiv.2506.10220](https://doi.org/10.48550/arXiv.2506.10220)
- Koda, J., Yagi, M., Yamanoi, H., & Komiyama, Y. 2015, *ApJ*, 807, L2, doi: [10.1088/2041-8205/807/1/L2](https://doi.org/10.1088/2041-8205/807/1/L2)
- Kravtsov, A. 2024, *The Open Journal of Astrophysics*, 7, 117, doi: [10.33232/001c.127487](https://doi.org/10.33232/001c.127487)
- Kroupa, P. 2001, *MNRAS*, 322, 231, doi: [10.1046/j.1365-8711.2001.04022.x](https://doi.org/10.1046/j.1365-8711.2001.04022.x)
- Laporte, C. F. P., Johnston, K. V., Gómez, F. A., Garavito-Camargo, N., & Besla, G. 2018, *MNRAS*, 481, 286, doi: [10.1093/mnras/sty1574](https://doi.org/10.1093/mnras/sty1574)
- Lazar, A., Bullock, J. S., Boylan-Kolchin, M., et al. 2020, *MNRAS*, 497, 2393, doi: [10.1093/mnras/staa2101](https://doi.org/10.1093/mnras/staa2101)
- Lazzarini, M., Williams, B. F., Durbin, M. J., et al. 2022, *ApJ*, 934, 76, doi: [10.3847/1538-4357/ac7568](https://doi.org/10.3847/1538-4357/ac7568)
- Leisman, L., Haynes, M. P., Janowiecki, S., et al. 2017, *ApJ*, 842, 133, doi: [10.3847/1538-4357/aa7575](https://doi.org/10.3847/1538-4357/aa7575)
- Liao, S., Gao, L., Frenk, C. S., et al. 2019, *MNRAS*, 490, 5182, doi: [10.1093/mnras/stz2969](https://doi.org/10.1093/mnras/stz2969)
- Lim, S., Côté, P., Peng, E. W., et al. 2020, *ApJ*, 899, 69, doi: [10.3847/1538-4357/aba433](https://doi.org/10.3847/1538-4357/aba433)
- Mancera Piña, P. E., Fraternali, F., Adams, E. A. K., et al. 2019, *ApJL*, 883, L33, doi: [10.3847/2041-8213/ab40c7](https://doi.org/10.3847/2041-8213/ab40c7)
- Marigo, P., Girardi, L., Bressan, A., et al. 2008, *A&A*, 482, 883, doi: [10.1051/0004-6361/20078467](https://doi.org/10.1051/0004-6361/20078467)
- Marleau, F. R., Habas, R., Poulain, M., et al. 2021, *A&A*, 654, A105, doi: [10.1051/0004-6361/202141432](https://doi.org/10.1051/0004-6361/202141432)
- McConnachie, A. W. 2012, *AJ*, 144, 4, doi: [10.1088/0004-6256/144/1/4](https://doi.org/10.1088/0004-6256/144/1/4)
- McConnachie, A. W., Huxor, A., Martin, N. F., et al. 2008, *ApJ*, 688, 1009, doi: [10.1086/591313](https://doi.org/10.1086/591313)
- McGaugh, S. S. 2005, *ApJ*, 632, 859, doi: [10.1086/432968](https://doi.org/10.1086/432968)
- McQuinn, K. B. W., Mao, Y.-Y., Buckley, M. R., et al. 2023, *ApJ*, 944, 14, doi: [10.3847/1538-4357/acaec9](https://doi.org/10.3847/1538-4357/acaec9)
- McQuinn, K. B. W., Skillman, E. D., Cannon, J. M., et al. 2009, *ApJ*, 695, 561, doi: [10.1088/0004-637X/695/1/561](https://doi.org/10.1088/0004-637X/695/1/561)
- . 2010, *ApJ*, 721, 297, doi: [10.1088/0004-637X/721/1/297](https://doi.org/10.1088/0004-637X/721/1/297)
- McQuinn, K. B. W., Skillman, E. D., Dolphin, A., et al. 2015, *ApJ*, 812, 158, doi: [10.1088/0004-637X/812/2/158](https://doi.org/10.1088/0004-637X/812/2/158)
- McQuinn, K. B. W., B. Newman, M. J., Savino, A., et al. 2024, *ApJ*, 961, 16, doi: [10.3847/1538-4357/ad1105](https://doi.org/10.3847/1538-4357/ad1105)
- Mei, S., Blakeslee, J. P., Côté, P., et al. 2007, *ApJ*, 655, 144, doi: [10.1086/509598](https://doi.org/10.1086/509598)
- Meier, D. S., Turner, J. L., & Beck, S. C. 2001, *AJ*, 122, 1770, doi: [10.1086/323136](https://doi.org/10.1086/323136)
- Méndez-Abreu, J., Ruiz-Lara, T., Sánchez-Menguiano, L., et al. 2017, *A&A*, 598, A32, doi: [10.1051/0004-6361/201629525](https://doi.org/10.1051/0004-6361/201629525)
- Merritt, A., van Dokkum, P., Danieli, S., et al. 2016, *ApJ*, 833, 168, doi: [10.3847/1538-4357/833/2/168](https://doi.org/10.3847/1538-4357/833/2/168)
- Mihos, J. C., Durrell, P. R., Ferrarese, L., et al. 2015, *ApJ*, 809, L21, doi: [10.1088/2041-8205/809/2/L21](https://doi.org/10.1088/2041-8205/809/2/L21)

- Montes, M., Infante-Sainz, R., Madrigal-Aguado, A., et al. 2020, *ApJ*, 904, 114, doi: [10.3847/1538-4357/abc340](https://doi.org/10.3847/1538-4357/abc340)
- Müller, O., Rich, R. M., Román, J., et al. 2019, *A&A*, 624, L6, doi: [10.1051/0004-6361/201935463](https://doi.org/10.1051/0004-6361/201935463)
- Niederste-Ostholt, M., Belokurov, V., Evans, N. W., & Peñarrubia, J. 2010, *ApJ*, 712, 516, doi: [10.1088/0004-637X/712/1/516](https://doi.org/10.1088/0004-637X/712/1/516)
- Oh, S.-H., de Blok, W. J. G., Brinks, E., Walter, F., & Kennicutt, Jr., R. C. 2011, *AJ*, 141, 193, doi: [10.1088/0004-6256/141/6/193](https://doi.org/10.1088/0004-6256/141/6/193)
- Okamoto, S., Arimoto, N., Ferguson, A. M. N., et al. 2015, *ApJL*, 809, L1, doi: [10.1088/2041-8205/809/1/L1](https://doi.org/10.1088/2041-8205/809/1/L1)
- Okamoto, S., Arimoto, N., Ferguson, A. M. N., Irwin, M. J., & Žemaitis, R. 2023, *ApJ*, 952, 77, doi: [10.3847/1538-4357/acdad1](https://doi.org/10.3847/1538-4357/acdad1)
- Oliphant, T. E. 2006, *A guide to NumPy*, Vol. 1 (Trelgol Publishing USA)
- Pace, A. B., Walker, M. G., Koposov, S. E., et al. 2021, *ApJ*, 923, 77, doi: [10.3847/1538-4357/ac2cd2](https://doi.org/10.3847/1538-4357/ac2cd2)
- Papastergis, E., Adams, E. A. K., & Romanowsky, A. J. 2017, *A&A*, 601, L10, doi: [10.1051/0004-6361/201730795](https://doi.org/10.1051/0004-6361/201730795)
- Pearson, S., Besla, G., Putman, M. E., et al. 2016, *MNRAS*, 459, 1827, doi: [10.1093/mnras/stw757](https://doi.org/10.1093/mnras/stw757)
- Pearson, S., Privon, G. C., Besla, G., et al. 2018, *MNRAS*, 480, 3069, doi: [10.1093/mnras/sty2052](https://doi.org/10.1093/mnras/sty2052)
- Peng, E. W., & Lim, S. 2016, *ApJ*, 822, L31, doi: [10.3847/2041-8205/822/2/L31](https://doi.org/10.3847/2041-8205/822/2/L31)
- Pontzen, A., & Governato, F. 2012, *MNRAS*, 421, 3464, doi: [10.1111/j.1365-2966.2012.20571.x](https://doi.org/10.1111/j.1365-2966.2012.20571.x)
- Prole, D. J., van der Burg, R. F. J., Hilker, M., & Davies, J. I. 2019, *MNRAS*, 488, 2143, doi: [10.1093/mnras/stz1843](https://doi.org/10.1093/mnras/stz1843)
- Radburn-Smith, D. J., de Jong, R. S., Seth, A. C., et al. 2011, *ApJS*, 195, 18, doi: [10.1088/0067-0049/195/2/18](https://doi.org/10.1088/0067-0049/195/2/18)
- Rusakov, V., Monelli, M., Gallart, C., et al. 2021, *MNRAS*, 502, 642, doi: [10.1093/mnras/stab006](https://doi.org/10.1093/mnras/stab006)
- Safarzadeh, M., & Scannapieco, E. 2017, *ApJ*, 850, 99, doi: [10.3847/1538-4357/aa94c8](https://doi.org/10.3847/1538-4357/aa94c8)
- Savino, A., Weisz, D. R., Skillman, E. D., et al. 2023, *arXiv e-prints*, arXiv:2305.13360, doi: [10.48550/arXiv.2305.13360](https://doi.org/10.48550/arXiv.2305.13360)
- Schombert, J., & McGaugh, S. 2014, *PASA*, 31, e036, doi: [10.1017/pasa.2014.32](https://doi.org/10.1017/pasa.2014.32)
- Sersic, J. L. 1968, *Atlas de Galaxias Australes*
- Siegel, M. H., Dotter, A., Majewski, S. R., et al. 2007, *ApJL*, 667, L57, doi: [10.1086/522003](https://doi.org/10.1086/522003)
- Silich, S., Lozinskaya, T., Moiseev, A., et al. 2006, *A&A*, 448, 123, doi: [10.1051/0004-6361:20053326](https://doi.org/10.1051/0004-6361:20053326)
- Skillman, E. D., Monelli, M., Weisz, D. R., et al. 2017, *ApJ*, 837, 102, doi: [10.3847/1538-4357/aa60c5](https://doi.org/10.3847/1538-4357/aa60c5)
- Smercina, A., Bell, E. F., Price, P. A., et al. 2020, *ApJ*, 905, 60, doi: [10.3847/1538-4357/abc485](https://doi.org/10.3847/1538-4357/abc485)
- Smithsonian Astrophysical Observatory. 2000, *SAOImage DS9: A utility for displaying astronomical images in the X11 window environment*. <http://ascl.net/0003.002>
- Telford, O. G., Dalcanton, J. J., Williams, B. F., et al. 2020, *ApJ*, 891, 32, doi: [10.3847/1538-4357/ab701c](https://doi.org/10.3847/1538-4357/ab701c)
- Toloba, E., Sand, D. J., Spekkens, K., et al. 2016, *ApJ*, 816, L5, doi: [10.3847/2041-8205/816/1/L5](https://doi.org/10.3847/2041-8205/816/1/L5)
- Toloba, E., Lim, S., Peng, E., et al. 2018, *ApJ*, 856, L31, doi: [10.3847/2041-8213/aab603](https://doi.org/10.3847/2041-8213/aab603)
- Toloba, E., Sales, L. V., Lim, S., et al. 2023, *ApJ*, 951, 77, doi: [10.3847/1538-4357/acd336](https://doi.org/10.3847/1538-4357/acd336)
- Torrealba, G., Belokurov, V., Koposov, S. E., et al. 2019, *MNRAS*, 488, 2743, doi: [10.1093/mnras/stz1624](https://doi.org/10.1093/mnras/stz1624)
- van der Burg, R. F. J., Hoekstra, H., Muzzin, A., et al. 2017, *A&A*, 607, A79, doi: [10.1051/0004-6361/201731335](https://doi.org/10.1051/0004-6361/201731335)
- Van Der Walt, S., Colbert, S. C., & Varoquaux, G. 2011, *Computing in Science & Engineering*, 13, 22
- van Dokkum, P., Danieli, S., Abraham, R., Conroy, C., & Romanowsky, A. J. 2019, *ApJL*, 874, L5, doi: [10.3847/2041-8213/ab0d92](https://doi.org/10.3847/2041-8213/ab0d92)
- van Dokkum, P., Abraham, R., Brodie, J., et al. 2016, *ApJ*, 828, L6, doi: [10.3847/2041-8205/828/1/L6](https://doi.org/10.3847/2041-8205/828/1/L6)
- van Dokkum, P., Danieli, S., Cohen, Y., et al. 2018, *Nature*, 555, 629, doi: [10.1038/nature25767](https://doi.org/10.1038/nature25767)
- van Dokkum, P., Shen, Z., Keim, M. A., et al. 2022, *Nature*, 605, 435, doi: [10.1038/s41586-022-04665-6](https://doi.org/10.1038/s41586-022-04665-6)
- van Dokkum, P. G., Abraham, R., Merritt, A., et al. 2015a, *ApJ*, 798, L45, doi: [10.1088/2041-8205/798/2/L45](https://doi.org/10.1088/2041-8205/798/2/L45)
- van Dokkum, P. G., Romanowsky, A. J., Abraham, R., et al. 2015b, *ApJ*, 804, L26, doi: [10.1088/2041-8205/804/1/L26](https://doi.org/10.1088/2041-8205/804/1/L26)
- Van Nest, J. D., Munshi, F., Wright, A. C., et al. 2022, *ApJ*, 926, 92, doi: [10.3847/1538-4357/ac43b7](https://doi.org/10.3847/1538-4357/ac43b7)
- Vasiliev, E., Belokurov, V., & Erkal, D. 2021, *MNRAS*, 501, 2279, doi: [10.1093/mnras/staa3673](https://doi.org/10.1093/mnras/staa3673)
- Virtanen, P., Gommers, R., Oliphant, T. E., et al. 2020, *Nature Methods*, 17, 261, doi: [10.1038/s41592-019-0686-2](https://doi.org/10.1038/s41592-019-0686-2)
- Žemaitis, R., Ferguson, A. M. N., Okamoto, S., et al. 2023, *MNRAS*, 518, 2497, doi: [10.1093/mnras/stac3133](https://doi.org/10.1093/mnras/stac3133)
- Walker, M. G., & Peñarrubia, J. 2011, *ApJ*, 742, 20, doi: [10.1088/0004-637X/742/1/20](https://doi.org/10.1088/0004-637X/742/1/20)
- Walter, F., Weiss, A., Martin, C., & Scoville, N. 2002, *AJ*, 123, 225, doi: [10.1086/324633](https://doi.org/10.1086/324633)
- Watts, C., Barway, S., Bait, O., & Wadadekar, Y. 2024, *A&A*, 691, L13, doi: [10.1051/0004-6361/202452002](https://doi.org/10.1051/0004-6361/202452002)
- Weisz, D. R., Dolphin, A. E., Skillman, E. D., et al. 2014, *ApJ*, 789, 147, doi: [10.1088/0004-637X/789/2/147](https://doi.org/10.1088/0004-637X/789/2/147)
- . 2015, *ApJ*, 804, 136, doi: [10.1088/0004-637X/804/2/136](https://doi.org/10.1088/0004-637X/804/2/136)

- Weisz, D. R., Skillman, E. D., Cannon, J. M., et al. 2008, ApJ, 689, 160, doi: [10.1086/592323](https://doi.org/10.1086/592323)
- Weisz, D. R., Dalcanton, J. J., Williams, B. F., et al. 2011, ApJ, 739, 5, doi: [10.1088/0004-637X/739/1/5](https://doi.org/10.1088/0004-637X/739/1/5)
- Weisz, D. R., Zucker, D. B., Dolphin, A. E., et al. 2012, ApJ, 748, 88, doi: [10.1088/0004-637X/748/2/88](https://doi.org/10.1088/0004-637X/748/2/88)
- Williams, B. F., Dalcanton, J. J., Stilp, A., et al. 2010, ApJ, 709, 135, doi: [10.1088/0004-637X/709/1/135](https://doi.org/10.1088/0004-637X/709/1/135)
- Williams, B. F., Lang, D., Dalcanton, J. J., et al. 2014, ApJS, 215, 9, doi: [10.1088/0067-0049/215/1/9](https://doi.org/10.1088/0067-0049/215/1/9)
- Williams, B. F., Dolphin, A. E., Dalcanton, J. J., et al. 2017, ApJ, 846, 145, doi: [10.3847/1538-4357/aa862a](https://doi.org/10.3847/1538-4357/aa862a)
- Yagi, M., Koda, J., Komiyama, Y., & Yamanai, H. 2016, The Astrophysical Journal Supplement Series, 225, 11, doi: [10.3847/0067-0049/225/1/11](https://doi.org/10.3847/0067-0049/225/1/11)
- Yozin, C., & Bekki, K. 2015, MNRAS, 452, 937, doi: [10.1093/mnras/stv1073](https://doi.org/10.1093/mnras/stv1073)
- Yun, M. S., Ho, P. T. P., & Lo, K. Y. 1994, Nature, 372, 530, doi: [10.1038/372530a0](https://doi.org/10.1038/372530a0)
- Zaritsky, D., Donnerstein, R., Dey, A., et al. 2023, ApJS, 267, 27, doi: [10.3847/1538-4365/acdd71](https://doi.org/10.3847/1538-4365/acdd71)